Applications in Energy and Combustion Science 23 (2025) 100356

Contents lists available at ScienceDirect

Applications in Energy and Combustion Science

journal homepage: www.elsevier.com/locate/jaecs

Lean Blow-Out analysis for the performance assessment of advanced burner designs operating under CO_2-diluted air conditions using a high-fidelity CFD approach

Gianmarco Lemmi [a,*], Simone Castellani [a], Roberto Meloni [b], Sofia Galeotti [a], Antonio Andreini [a]

[a] Department of Industrial Engineering, University of Florence, Via S. Marta, 3, Florence, 50139, Italy
[b] Baker Hughes, Via F. Matteucci 2, Florence, 50127, Italy

ARTICLE INFO

Keywords:
LBO
LES
FGM
EGR
Industrial lean-premixed burner
Natural gas combustion modelling

ABSTRACT

Amid the growing focus on sustainable industrial practices, Carbon Capture and Storage (CCS) systems are becoming increasingly essential for reducing the carbon footprint of Gas Turbine (GT) power generation. In this context, an efficient GT-CCS coupling can be achieved by employing high Exhaust Gas Recirculation (EGR) rates to boost CO_2 content at the CCS inlet. However, the reduced oxygen levels resulting from these operating conditions pose significant challenges to conventional combustion systems, limiting flame stability and, consequently, engine operability. Overcoming these challenges requires the development of novel technical solutions aimed at enhancing combustor performance under high EGR rates.

Computational Fluid Dynamics (CFD) is crucial in this endeavour offering detailed analysis of intricate flow behaviours, mixing process dynamics, flame structures, and stability thresholds within the combustor. Given the demand for extensive simulations to assess flame stability across various burner designs and operating conditions, balancing the necessity for high accuracy while keeping computational expenses in check is mandatory.

This study employs a high-fidelity CFD approach to perform a comprehensive Lean Blow-Out (LBO) analysis, with the goal of identifying burner designs that exhibit broader operability limits under highly CO_2-diluted air conditions, which emulate the effects of a real EGR system. All simulations utilise an extended Flamelet Generated Manifold (FGM) turbulent combustion model, whose accuracy and cost-effectiveness have been previously validated by the authors.

The numerical results demonstrate the capability of CFD to identify unique blow-off dynamics that are challenging to observe experimentally. Additionally, the findings highlight the most effective design strategy for extending the flame stability range under high EGR levels.

1. Introduction

In the ongoing global energy transition towards carbon neutrality [1], driven by the goals of the Paris Agreement [2], reducing emissions from existing power plants remains critical. In power generation, gas turbines primarily rely on natural gas, which, although cleaner than coal and oil (22% of emissions vs. 45% and 33%, respectively [3,4]), still falls short of mid-century neutrality targets. Further reductions are difficult to achieve through efficiency gains alone due to thermodynamic limits, making a shift to carbon-free fuels, especially hydrogen, essential [5]. However, hydrogen adoption is hindered by infrastructure and production constraints [6–9]. Interim solutions are therefore needed to lower emissions from conventional fuels while supporting the gradual integration of cleaner alternatives. These aim to enable co-firing with carbon-free fuels and reduce CO_2 and NO_x emissions.

Carbon Capture and Storage (CCS) is a leading interim option for cutting CO_2 emissions from gas turbines [10,11]. Effective CCS integration requires high Exhaust Gas Recirculation (EGR) rates to enrich CO_2 at the capture unit inlet [12–16], resulting in reduced oxygen concentration within the combustor and associated operational challenges [17]. Specifically, recirculated flue gas increases CO_2 and N_2 levels in the oxidiser, affecting flame stability [18–20]. Evulet et al. [21] showed that the commercial GE's 9FB DLN nozzle can operate stably with up to 30% EGR at full load, and potentially 40% with minor design modifications. Similar findings in [17] suggest that up to 35% EGR is feasible with existing DLN combustors, especially

* Corresponding author.
E-mail address: gianmarco.lemmi@unifi.it (G. Lemmi).

https://doi.org/10.1016/j.jaecs.2025.100356
Received 18 April 2025; Received in revised form 7 July 2025; Accepted 13 July 2025
Available online 5 August 2025

with pilot fuel support. Staged combustion also offers improved flame stability under these conditions [22,23].

In addition to EGR-based strategies, oxyfuel combustion, where methane is burned in oxygen with CO_2 as the primary working fluid, has gained significant attention for its potential to achieve near-zero NO_x and CO_2 emissions [24]. This approach can be seen as an “extreme” form of EGR, operating in a nearly nitrogen-free environment with flue gases mainly composed of CO_2 and H_2O, leading to unique flame dynamics and stability challenges. The high CO_2 content acts as an effective diluent, reducing flame temperature, controlling thermal loads on turbine components, and suppressing pollutant formation. Several oxyfuel gas turbine combined cycle concepts have already been proposed to exploit these advantages [25–27].

The European-founded project TRANSITION [28] - *fuTure hydRogen Assisted gas turbiNeS for effective carbon capTure IntegratiON* - aims to address the challenge of ensuring stable and efficient combustion under high CO_2-diluted conditions typical of advanced EGR systems. In this context, Computational Fluid Dynamics (CFD) has the potential to play a crucial role in identifying flame stability limits across various EGR levels and burner configurations. However, industry demands pose a dual challenge: the need for a robust turbulent combustion model capable of accurately addressing near-blow-out phenomena, and the requirement for extensive CFD simulations during the design phase to evaluate the impact of different technical solutions on flame stability across varying EGR levels, emphasising the imperative to manage computational costs.

In this study, an enhanced version of the FGM model, previously validated by the authors [29,30], is employed to address both objectives. The primary goal of this work is to conduct a comprehensive Lean Blow-Out (LBO) analysis through a Large Eddy Simulation (LES) approach, assessing flame stability across different burner design solutions under heavy CO_2-diluted air conditions. The numerical results are benchmarked against experimental data from an LBO test campaign conducted by the THT Lab of the University of Florence, providing a robust evaluation of the accuracy and reliability of the proposed approach. The experimental test rig and the computational setup will be outlined in the subsequent section, followed by a description of the numerical LBO procedure. The Results and Discussion will offer a direct comparison of volume-averaged chamber temperature and flame topology among the different design burners investigated. This evaluation will help identify the burner geometries with the most promising performance, which will be recommended for further advanced experimental validation.

2. Lean-Blow Out phenomenology

Lean Blowout (LBO) limits low-emission operation in gas turbine combustors, arising from the failure of flame stabilisation due to the interplay of chemical heat release, fluid dynamics, and, in liquid fuels, spray atomisation and evaporation. The transition to blowout follows a multistage process involving both local and global phenomena [31, 32], and despite extensive research, its mechanisms remain partially understood, with multiple theories proposed [33–36]. A recent, experimentally supported flamelet-based view attributes blowout onset to aerodynamic stretch and localised heat loss eroding the flame front until global flame extinction occurs [37,38].

In turbulent bluff-body stabilised flames, this erosion begins with local extinctions in high-strain shear layers, disrupting the flame front and, over time, compromising the ability of recirculation zones to sustain combustion [31]. This process unfolds over timescales longer than flow residence time [39], revealing a gradual decay of flame surface density and increased front curvature near extinction [40]. Recent approaches have linked the onset of blowout to threshold values of the Karlovitz number, offering a physically grounded criterion for extinction onset in turbulent premixed conditions [41].

Swirl-stabilised flames add complexity through vortex breakdown and the formation of inner and outer recirculation zones, cycling hot combustion products to help anchor and stabilise the flame. However, near blowout, perturbations such as cold reactants entering the inner recirculation have been observed to trigger flame extinction [42]. Studies using high-speed diagnostics and numerical simulations have revealed that flame stabilisation in swirled systems involves competing dynamics between the flame root near the lower stagnation point and a helical branch aligned with the precessing vortex core [43]. Extinction is often characterised by the inability of the flame to re-ignite across the shear layer, leading to flame root detachment and global blowout.

Several studies have demonstrated that pilot flames and hydrogen enrichment significantly affect LBO limits [44–46]. For instance, pilot jets near the flame root improve flameholding capacity due to enhanced local heating, radical generation, and turbulence. Furthermore, the pilot increases the local Damköhler number and creates a recirculation of high-temperature gases, reducing the ignition delay of the main flame front [47]. Muruganandam et al. [48] experimentally showed that in a swirl burner with pilot injection, blowout is preceded by the loss of the main flame while the pilot persists, followed by intermittent reignition events. These fluctuating ignition-extinction cycles can delay total blowout and indicate proximity to LBO. Recent work by Guiberti [49] highlights the crucial role of pilot composition and momentum flux. Hydrogen-enriched pilots notably improve blowout margins via faster kinetics and enhanced radical generation. However, while pilots extend stability, they also introduce richer zones that can increase NO_x emissions [50,51]. Thus, understanding pilot-main flame interactions is essential for both blowout prevention and optimising efficiency and emissions.

While the LBO limit in swirl flames is influenced by multiple factors, including swirl number and direction, fuel composition, and inlet temperature [52–54], it remains hard to predict due to the nonlinear flow-reaction coupling. In practice, blowout proximity is often detected via low-frequency combustion oscillations [55,56], though these indicators need careful calibration and are not always reliable [43]. Therefore, advancing the fundamental understanding of blowout in complex systems is vital for developing next-generation low-emission combustors.

3. Experimental test rig and operating conditions

3.1. Burner geometry

The burner concept under investigation is a state-of-the-art lean premixed design developed by Baker Hughes for heavy-duty gas turbine applications. The burner is supplied with fuel through two separate lines [57], as schematically depicted in Fig. 1. The fuel injected through

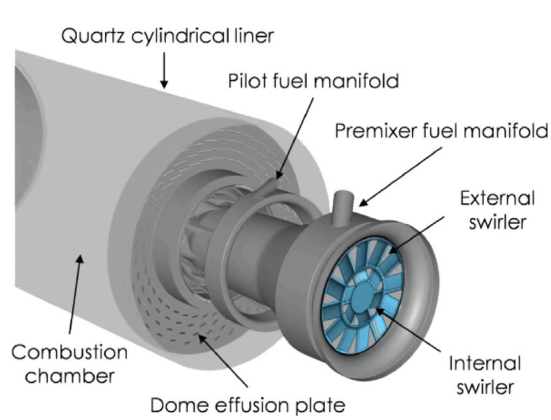

Fig. 1. Schematics of Baker Hughes’ burner. Swirler representation is simplified for confidentiality.

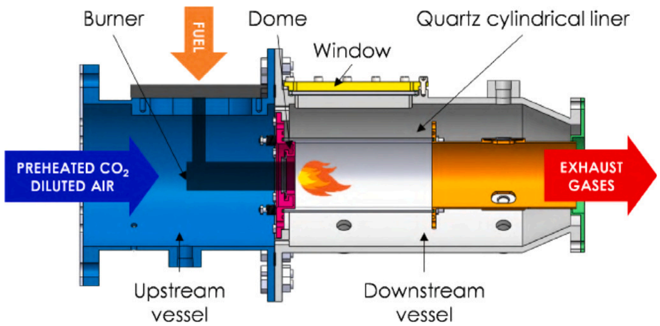

Fig. 2. Schematics of the THT Lab reactive test cell [50,58].

Table 1
LBO starting test point operating conditions.

Quantity	Unit	Value
Op. pressure	[Pa]	101 325
T_{oxid}	[K]	578
T_{fuel}	[K]	291
Oxid. comp.	[%vol]	67.16 N_2, 18.08 O_2, 13.96 CO_2, 0.8 Ar
Fuel comp.	[%vol]	90.32 CH_4, 6.06 C_2H_6, 1.99 C_3H_8, 0.68 C_4H_{10}, 0.95 N_2
Sim. EGR lv	[%]	50
Pilot split	[%]	30
$\Delta P/P$	[%]	4.2

the first manifold mixes with the oxidiser flow via a counter-rotating swirler, ensuring uniform mixture delivery into the combustion chamber. In contrast, the pilot line stabilises the flame by directly delivering gas into the primary zone through circumferentially distributed holes.

3.2. Experimental test rig

The burner was investigated in the optically accessible reactive test cell of the THT Lab of the University of Florence, whose schematics are outlined in Fig. 2.

The test article is engineered to facilitate optical flame analysis while offering adaptability for various burner configurations. The external casing features an upstream vessel that accommodates the burner's entry point, and a downstream section equipped with a pair of perpendicular viewing ports, the latter strategically positioned to enable comprehensive flame visualisation.

The combustion chamber has an internal diameter of 110 mm and extends approximately 2.5 times its diameter. The combustor liner is a 2.5 mm thick cylindrical structure made of quartz, while the downstream flame tube liner is constructed from 2 mm thick stainless steel. The entire flame tube is cooled by forced convection, using a portion of the incoming air that flows through the annulus between the liner and the confining vessel, bypassing the combustion process. The same air is also employed to maintain the temperature of the optical windows. In addition, the dome plate is cooled by a series of inclined effusion holes.

Concerning flow measurements, the rig is outfitted with an array of sensors. Thermocouples and static pressure probes are strategically placed throughout the system, providing real-time data on flow parameters. A HORIBA PG-350 gas analyser is plunged into the downstream flame tube to extract the exhaust gas for detailed emissions analysis, with sampling occurring after approximately 9 ms of residence time. This allows for accurate quantification of key pollutants, with a particular focus on CO and NO_x. For those seeking more in-depth information on the design specifications and instrumentation details of the rig, additional resources are available in related publications from the authors [50,58].

The rig operates at standard atmospheric pressure, utilising CO_2-diluted air to simulate EGR-like conditions. The decision to use CO_2-enriched mixtures arises from the practical challenges associated with recreating authentic EGR conditions or employing N_2-enriched alternatives on a laboratory scale, mainly due to cost constraints and volume requirements. Although there are differences between CO_2 dilution and real (dry) EGR, CO_2 dilution is recognised as a more demanding condition for flame stability than actual EGR [59]. Consequently, this conservative approach provides a robust compromise for the initial design and investigation phase, establishing a solid foundation for subsequent optimisation efforts. In particular, tests are conducted with a 14% CO_2 dilution in volume, which is intended to simulate the effects of an EGR level of approximately 50%. According to the fuel composition measured during experimental tests, the natural gas used in this setup featured a high C_2+ (multi-carbon hydrocarbons) content – approximately 9% by volume – with ethane (C_2H_6), propane (C_3H_8), and butane (C_4H_{10}) identified among the heavier hydrocarbons. The fuel enters the system at a temperature of 291 K, while the airflow is first dehumidified using a drying unit and then preheated to 578 K by an electric heater. A constant air mass flow rate of 320 g/s is injected through the plenum, including the component dedicated to liner cooling. To achieve the target thermal power output of approximately 74 kW, the total fuel mass flow rate is adjusted accordingly, with 30% of it directed through the pilot line. A modulating valve is employed to ensure a consistent pressure drop ($\Delta P/P$) of around 4.2% across the combustor.

The above operating conditions define the starting test point for lean blow-out analysis and are summarised in Table 1.

Under these conditions, the Reynolds number at the burner exit, based on the bulk velocity, burner diameter, and local mixture properties, is approximately 56,000, indicating a fully turbulent flow regime.

4. Numerical setup

To capture the unsteady and localised flame dynamics near lean blow-out, simulations were carried out using the commercial code ANSYS Fluent® 2022 R1 with a high-fidelity LES approach, as steady-state models are insufficient for this purpose. Unresolved turbulence effects are modelled using the Wall-Adapting Local Eddy-Viscosity (WALE) sub-grid scale formulation [60], selected for its cost-effectiveness in reconstructing the correct asymptotic behaviour of wall-bounded flows [61]. The segregated Pressure-Implicit with Splitting of Operators (PISO) algorithm [62,63] is employed for pressure–velocity coupling, minimising the number of sub-iterations required per time-step to achieve convergence [64]. For spatial discretisation, a second-order upwind scheme is applied to all variables except momentum fluxes, where a bounded central differencing scheme is used. Time integration is performed using an implicit second-order scheme with a time step of 1×10^{-5} s, allowing CFL numbers up to 3 in the regions of interest. This choice is supported by a previous time-step sensitivity analysis by the authors, in which simulations with CFL numbers well below 1 showed negligible differences in flame shape prediction, thereby justifying the adoption of this more computationally efficient setup.

In the context of LBO analysis, it is imperative to capture the primary flame-quenching mechanisms, as they directly influence flame dynamics under conditions of low reactivity, leading to phenomena such as flame lift-off and elongation. Simultaneously, the burner design phase demands several numerical simulations to assess how different technical solutions affect flame stability under specific CO_2 dilution levels, i.e., EGR levels. To this end, an enhanced version of the Flamelet Generated Manifold (FGM) turbulent combustion model is employed, featuring an extended Finite-Rate (FR) closure that incorporates stretch and heat loss effects [65]. The rationale behind choosing this enhanced yet tabulated chemistry approach lies in the higher computational efficiency of the FGM method compared to models from the species

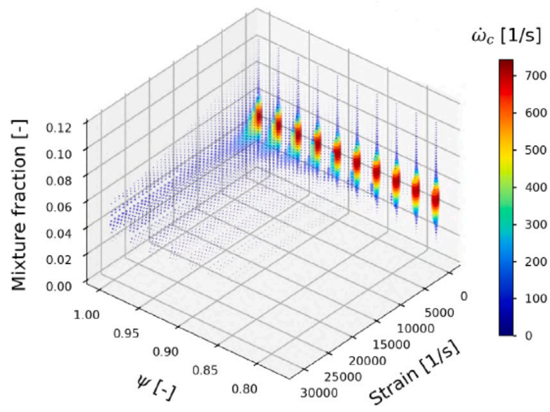

Fig. 3. Finite-Rate turbulent progress variable source term ($\dot{\omega}_c$) within the mixture fraction, strain, and heat loss 3D space.

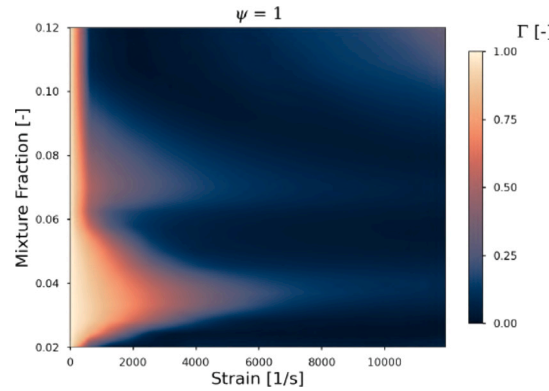

Fig. 4. Γ table in the mixture fraction and strain space for the adiabatic condition ($\psi = 1$).

transport approach family, specifically the Artificially Thickened Flame (ATF) model. In previous work by the authors [29,30], it was demonstrated that while the ATF model yielded results very similar to those of the FGM approach, its computational cost was approximately six times higher. Given that the LBO analysis involves simulating long time frames with multiple changes in inlet boundary conditions, as described in the following sections, the FGM model was selected for its balance between computational efficiency and the ability to capture local extinction phenomena. Further details are provided in the next subsection.

4.1. Turbulent combustion modelling

The FGM approach is a widely used turbulent combustion model within the flamelet framework [66]. This model represents turbulent flames as an ensemble of laminar, one-dimensional flamelets embedded in the turbulent flow field. During FGM pre-processing, laminar flamelets are solved to create a multi-dimensional manifold where thermodynamic variables depend solely on two control variables: the mixture fraction (Z) and the reaction progress variable (c) [67]. For this study, a 64 × 32 look-up table in $Z \times c$ space is generated by solving premixed flamelets in ANSYS Fluent® with the GRI-Mech 3.0 mechanism, which includes 53 species and 325 reactions [68]. The mixture fraction is based on Bilger's formulation [69], and the reaction progress variable is normalised as $Y_c = Y_{CO_2} + Y_{CO}$ relative to its equilibrium value. Turbulence–chemistry interactions are represented by mass-weighted β-PDFs of Z and c ($\tilde{P}(Z,c)$) [70], requiring transport equations for both mean values and variances of Z and c. In LES, however, the mixture fraction variance is modelled using an algebraic expression rather than a dedicated transport equation [64]. To improve efficiency, a pre-integrated turbulent look-up table is PDF-averaged during pre-processing, replacing run-time integration with computationally efficient interpolation. For further details on the FGM model's mathematical foundation, refer to Ramaekers et al. [71].

This study employs an extended version of the Finite-Rate (FR) closure, initially proposed by Klarmann et al. [72,73] within the RANS framework and subsequently adapted to an LES context by Langone et al. [65], to compute the Reynolds-averaged source term for the reaction progress variable. Specifically, a correction factor Γ, which accounts for the effects of strain (a) and heat loss (ψ), is applied to the standard Finite-Rate turbulent reaction progress variable source term ($\overline{\omega}_c$), effectively reducing the overall reactivity of the combustion process. The adjusted reaction progress source term ($\overline{\omega}_c^*$) is calculated as follows:

$$\overline{\omega}_c^* = \Gamma(Z,a,\psi) \quad \underbrace{\bar{\rho} \iint \frac{\dot{\omega}_c(Z,c)}{\rho(Z,c)} \tilde{P}(Z,c)\, dZ\, dc}_{\text{Standard FR turbulent } c \text{ source term } (\overline{\omega}_c)} \tag{1}$$

where $\dot{\omega}_c$ is directly extracted from the laminar flamelets' look-up table. To determine Γ, several freely propagating flames (zero strain) and premixed counterflow flames (strained) are solved using the Cantera libraries [74] to generate a 3D map for $\dot{\omega}_c$ in the mixture fraction (Z), strain (a), and heat loss (ψ) space, as shown in Fig. 3. Then, $\Gamma(Z,a,\psi)$ is defined as the ratio between the maximum value of the strained, non-adiabatic progress variable source term and the adiabatic, unstrained one in a 1D laminar flame:

$$\Gamma(Z,a,\psi) = \frac{\max \dot{\omega}_c(Z,a,\psi)}{\max \dot{\omega}_c^0(Z)} \tag{2}$$

where ψ represents the heat loss parameter, defined as the temperature deficit of the burnt gas relative to the corresponding equilibrium temperature, and a represents the strain rate, calculated from the velocities of the opposing jets. A 2D contour map of Γ for the adiabatic case ($\psi = 1$) is reported in Fig. 4.

At the start of the CFD simulation, the table is loaded into memory via a custom C-language subroutine. The computed values of stretch, heat loss, and mixture fraction are then used to query the table at runtime for each domain cell. Since stretch and heat loss are not inherently included in the FGM framework, a tailored modelling approach is required, as described in the following section.

4.2. CFD: computing stretch and heat loss

Stretch (κ) and heat loss (ψ) are computed using analytical expressions embedded in a C-based User Defined Function (UDF), dynamically called at each time step within ANSYS Fluent®. Here, stretch (κ), formally defined as the rate of the flame surface variation per unit area [75], is expressed as a combination of resolved strain ($\tilde{a}_{\text{res}}$), sub-grid scale strain ($\tilde{a}_{\text{sgs}}$), and curvature (σ_c) effects:

$$\kappa = \frac{1}{A}\frac{dA}{dt} = (\delta_{ij} - n_i\tilde{n}_j)\frac{\partial \tilde{u}_i}{\partial x_j} + \Gamma_\kappa \frac{\sqrt{k_{\text{sgs}}}}{\Delta} + S_l \frac{\partial \tilde{n}_i}{\partial x_i} = \tilde{a}_{\text{res}} + \tilde{a}_{\text{sgs}} + \sigma_c \tag{3}$$

where A is the surface area of an infinitesimal flame surface element, δ_{ij} is the Kronecker delta, n is the normal vector to the flame front, Γ_k is an efficiency function [76], k_{sgs} is the sub-grid kinetic energy, and S_l is the laminar flame speed.

According to Eq. (3), flame stretch is calculated as the sum of strain and curvature effects. It is important to note that the flame's response to stretch is determined solely by the magnitude of this combined effect, regardless of how strain and curvature are distributed. This allows the use of premixed counterflow flames, characterised by pure strain, as a representative configuration when generating the Γ table, effectively modelling the influence of both strain and curvature. As also evident from Eq. (3), flame stretch can assume both positive and negative values. However, since the FGM library is constructed using

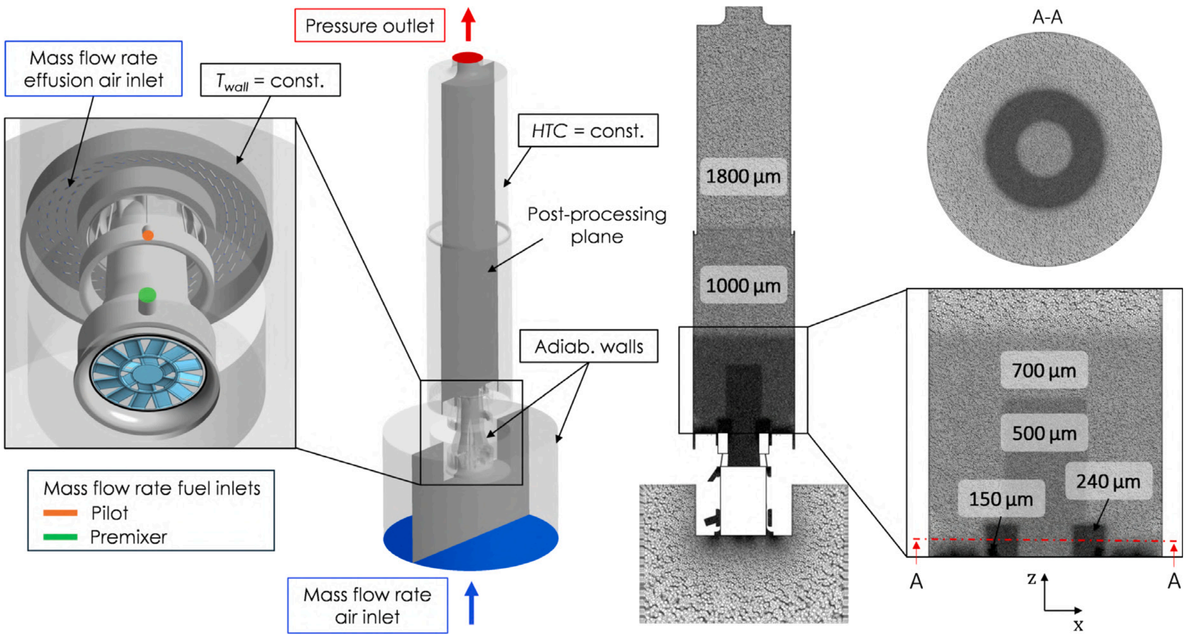

Fig. 5. Computational grid on a plane intersecting two axes of the pilot fuel line (post-processing section). The mesh resolution is enhanced within the swirler and the primary zone regions, with its peak in the pilot fuel injection for a refined characterisation of the mixing process. Design details omitted.

counterflow diffusion flames, which only provide tabulated data for positive strain rates, the influence of negative stretch is neglected in the current modelling approach. Specifically, for $\kappa < 0$, the consumption rate is assumed to equal that at $\kappa = 0$, i.e., $\dot{\omega}_c(\kappa < 0) = \dot{\omega}_c(\kappa = 0)$. Despite this strong approximation, the primary objective is to make the FGM model responsive to local flame quenching phenomena associated with high positive strain rates. This rationale underpins the adopted assumption, which has been validated in previous studies [65,77,78].

Regarding heat loss, ψ represents the temperature deficit in the burnt gases (products) of laminar counterflow flamelets, corresponding to the condition where $c = 1$ and $c''^2 = 0$. Within the CFD framework, as dictated by the FGM model, the progress variable c ranges from 0 to 1 across the reactive flow field. Consequently, ψ must be formulated to allow for its calculation across the full range of the progress variable. To achieve this, ψ is expressed as the ratio of the local temperature to the local adiabatic flame temperature:

$$\psi = \frac{T_b}{T_{eq}} \simeq \frac{\tilde{T}(\tilde{Z}, \tilde{Z}''^2, \tilde{c}, \tilde{c}''^2, \tilde{h})}{\tilde{T}(\tilde{Z}, \tilde{Z}''^2, \tilde{c}, \tilde{c}''^2, \tilde{h}_{ad})} \tag{4}$$

In this non-adiabatic FGM approach, as shown in Eq. (4), mixture properties are formally defined as functions of five variables. To reduce table dimensionality, the non-adiabatic flamelet libraries in Fluent are constructed under the assumptions that species mass fractions are insensitive to enthalpy variations and that the variance of the progress variable can be neglected when evaluating thermodynamic properties, enabling reduced-order tabulation [64]. The local values of stretch (κ) and heat loss (ψ), computed using Eqs. (3)–(4), along with the mixture fraction values natively provided by the solver, are used to query the $\Gamma(Z, a, \psi)$ table stored in memory. The resulting value of Γ is then used to calculate the adjusted reaction progress source term. Additional information on this extended version of the FGM is available in [29,72].

4.3. Computational domain and boundary conditions

The numerical domain, depicted in Fig. 5, includes a portion of the rig upstream vessel that functions as an inlet plenum, the entire burner geometry, encompassing both the premixer and pilot fuel manifolds, the effusion cooling holes, the combustion chamber, and the discharge downstream flame tube. Due to confidentiality constraints, some specific design details within the burner are omitted. The computational grid is composed of a fully unstructured mesh, consisting of 22 million polyhedral cells, with mesh sizes of 500 µm within the burner and 700 µm in the primary zone. Local refinements are applied within the chamber to accurately capture mixing and flow dynamics. Specifically, an annular body of influence with a local mesh size of 240 µm is generated near the dome, along with local refinements of 150 µm at the pilot ducts' ends, ensuring a precise reconstruction of the fluid interaction between the pilot fuel and the premixed mixture from the swirler. A preliminary assessment of the LES grid resolution, conducted in a prior work by the authors [29], confirmed its adequacy, with Celik's LES quality index (LESIQ) values consistently exceeding 0.92 [79].

Regarding boundary conditions, the domain features two air inlets, one for the plenum and one for the effusion cooling holes, and two fuel inlets, for the premixer manifold and the pilot line, respectively. Constant mass flow rates and temperatures are specified for both fuel and air at the respective inlet patches, based on the data provided in Section 3.2, while the pressure-outlet boundary condition is set to match standard atmospheric conditions. With the imposed mass flow rates, a pressure drop of 4.2% is measured across the burner, perfectly aligning with the experimental operating conditions. A constant temperature boundary condition is imposed on the dome walls, while a convective heat transfer boundary condition is applied to the chamber and flame tube walls. The Heat Transfer Coefficient (HTC) value, determined through a dedicated test campaign, ensures an accurate reproduction of the wall temperatures observed during the experiments. The remaining walls are modelled as adiabatic. The use of the GRI-Mech 3.0 detailed mechanism allows for an exact match to the experimental fuel composition, as outlined in Table 1, except for propane, which was employed to represent both C_3H_8 and C_4H_{10}, due to species availability in the GRI-Mech 3.0 mechanism.

4.4. Numerical lean blow-out procedure

The primary objective of this analysis is to identify the burner geometry that offers the broadest flame operability under high levels of CO_2 dilution in the air. A logical initial approach in this context would be to conduct a blow-out analysis by progressively increasing the CO_2 concentration within the air. This "multi-stream" combustion scenario is inherently addressed by species transport models, such as the ATF model. However, because of the computational cost associated with the additional transport equations required to properly handle the chemistry, it has been excluded from consideration. On the other hand, a tabulated chemistry approach like the FGM, which relies on accurately resolving non-reactive mixing, does not natively support this strategy, thereby preventing analyses involving variations in the oxidiser or fuel composition. Therefore, instead of progressively increasing the CO_2 concentration in the air, the workflow of this analysis involves systematically reducing the fuel mass flow rate until lean blow-out occurs [78] while maintaining a fixed oxidiser composition with high CO_2 dilution levels. This approach avoids any changes in both fuel and oxidiser composition, allowing for the use of a standard PDF dimension. Although the two methods differ in their specifics, reducing the fuel mass flow rate demonstrates similar blow-out behaviour and offers comparable insights into flame stability, particularly under conditions of high CO_2 dilution. As a result, this LBO methodology was adopted in the current study to identify the burner configuration with the greatest flame stability at high EGR levels, ultimately supporting burner design.

The first step of the analysis consists of an LES of the given geometry under the starting test point operating conditions (Table 1), here identified as S0. All unsteady simulations are initialised from the respective preliminary Reynolds-Averaged Navier–Stokes (RANS) calculations, the latter featuring a $k-\epsilon$ Realizable turbulence model. LES simulations are then run for a time equivalent to 4 flow-through times (FTTs), each approximately 14 ms, before activating the averaging procedure. To ensure statistically converged results, 3 additional FTTs are simulated during this initial stage. Following stabilisation, a 10% reduction in fuel mass flow rate is applied, maintaining the pilot split constant at 30%. Since the air mass flow rate is kept constant throughout the entire simulation campaign, each reduction in fuel mass flow rate corresponds to a proportional decrease in the global equivalence ratio. Subsequent reductions of 5% in fuel mass flow rate are iteratively implemented until flame extinction occurs. Volume-averaged temperature and volume integral of heat release monitors are employed to identify the onset of LBO conditions [78]. It is noteworthy that every fuel mass flow rate drop is applied upon reaching a stable thermodynamic condition under the local boundary conditions.

The numerical procedure is consistent with the experimental practise, where a discrete fuel mass flow rate reduction is applied until reaching blow-out, the latter evaluated by monitoring the wall temperature from a thermocouple placed on the downstream flame tube.

5. Investigated burner design solutions

As outlined earlier, the numerical LBO procedure evaluates how different burner designs affect flame stability limits under high CO_2 dilution, simulating real EGR conditions. This procedure is systematically applied to five different burner geometries, each with specific pilot line and main premixer modifications.

5.1. Premixing duct and pilot line design

The first part of this work focuses on assessing the impact of two different fuel injection strategies occurring within the swirler, each linked to a specific premixing duct geometry, and four pilot line configurations on combustor aerodynamics and overall flame stability. Each tested geometry, denoted A0, B1, B2, and B3, employs the same counter-rotating swirler and features distinct design characteristics, as detailed below (Figs. 6–7–8):

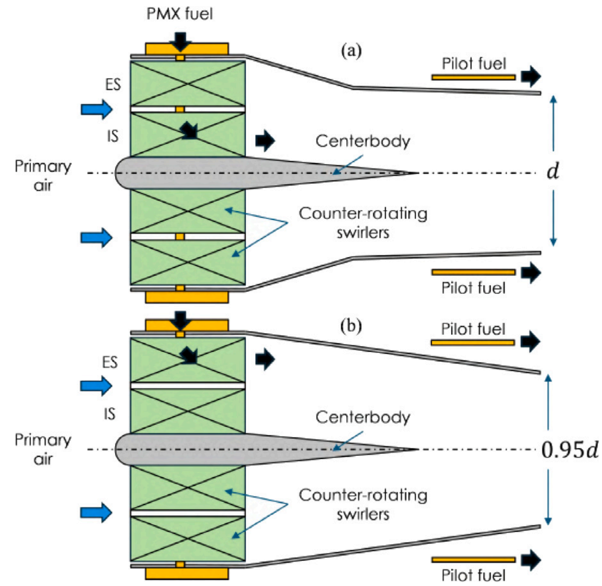

Fig. 6. Premixing duct geometries with (a) two-stage and (b) constant conical convergent sections. ES = external swirler; IS = inner swirler; PMX = premixer. Design details are omitted for clarity.

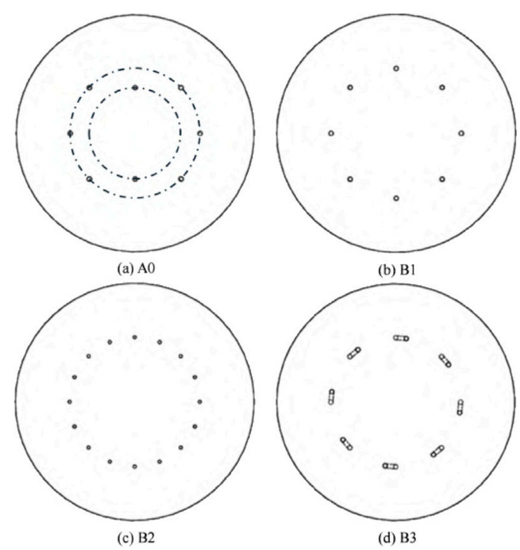

Fig. 7. Pilot ducts distribution on the dome.

- A0: This configuration serves as the baseline for the investigation and acts as the reference point for all subsequent comparisons. Fuel from the premixed line (PMX) is injected at the tip of the inner swirler through a narrow duct within the outer blades, allowing it to mix with the airflow through strong turbulence generated by the shear layer between the two swirlers. The premixing duct has a two-stage convergence, starting with a steeper angle near the swirler to direct the outer flow towards the duct centre and enhance mixing, followed by a more gradual taper towards the exit, as illustrated in Fig. 6a. The pilot line consists of N holes, each with an equal diameter D, arranged in a non-axisymmetric pattern around the burner (Fig. 7a). Notably, two holes are positioned on a smaller radius on the dome with distinct inward injection angles, while the remaining holes are directed outward (Fig. 8).
- B1: In this design variant, as with all subsequent configurations, fuel is injected directly at the tip of the outer swirler. The premixing duct maintains a constant conical convergence from the swirler to the exit section, with the exit diameter reduced by 5% compared to the corresponding section in the A0 geometry (Fig. 6b). This conical shape keeps the fuel near the wall, allowing it to efficiently feed the pilots upon entering the chamber, thereby

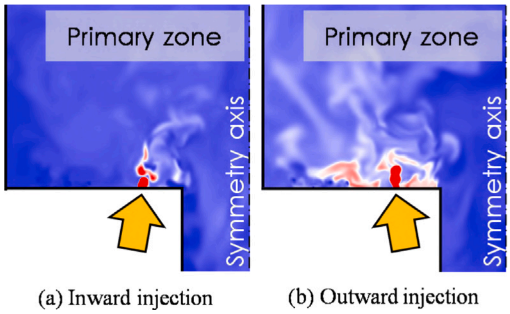

Fig. 8. Schematics of pilot fuel injection angles: (a) Inward-directed and (b) outward-directed. Design details omitted.

enhancing flame stabilisation. The pilot line consists of N holes of equal diameter D, arranged in a rotationally symmetric pattern around the burner, with all N pilot fuel injections directed outward (Fig. 7b).

- B2: This second pilot configuration features $2N$ smaller holes, each with a diameter of 0.7 D, arranged in an axisymmetric pattern (Fig. 7c). All holes direct their injections outward.
- B3: This design is similar to B1 but includes a modification where the holes are tilted in the direction of the swirled flow. This adjustment aims to reduce the strain experienced by the piloted flames, potentially enhancing flame stability and overall performance (Fig. 7d).

This comparative analysis aims to evaluate how variations in premixing duct and pilot line geometries impact flame stabilisation, particularly under challenging operating conditions with reduced oxygen content.

5.2. Swirler design

The final phase of this investigation evaluated an alternative main premixer design by replacing the counter-rotating swirler (Fig. 9a) with a co-rotating configuration (A0x, Fig. 9b), while retaining the same premixing duct and pilot line as in the A0 geometry. This modification aims to isolate the effect of a different flame stabilisation mechanism on the LBO limits.

In A0x, the preserved swirl number promotes a well-defined inner recirculation zone (IRZ), supporting a stable, V-shaped flame (Fig. 10). Although fuel is still injected through the pilot lines, the dominant aerodynamic anchoring reduces the visible influence of the pilot flame. Conversely, the counter-rotating swirler weakens the swirl, suppressing the IRZ and making the pilot flame essential for stabilisation under lean conditions. Comparing the two configurations thus reveals how differing stabilisation mechanisms – IRZ-driven versus pilot-assisted – affect flame stability under high CO_2 dilution. All tested design solutions are summarised in Table 2.

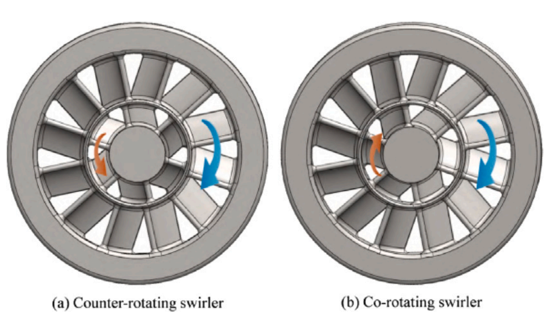

Fig. 9. Schematics of counter-rotating (a) and co-rotating swirlers (b). Illustrations do not depict the actual Baker Hughes geometry for confidentiality reasons.

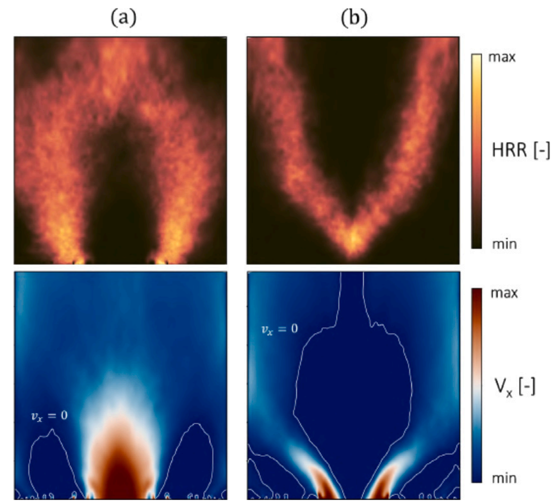

Fig. 10. Normalised time-averaged contours of heat release rate (HRR) and axial velocity (v_x) on the midplane section of the burner for the counter-rotating (a) and co-rotating (b) swirlers.

Table 2
Swirler and pilot configurations.

Configuration	A0	B1	B2	B3	A0x
Swirler					
Counter-rot.	X	X	X	X	
Co-rot.					X
PMX fuel injection					
Inner swirler	X				X
Outer swirler		X	X	X	
Pilots					
8 non-axisym.	X				X
8 axisym.		X			
16 axisym.			X		
8 axisymm. tilted				X	

6. Results and discussion

This section presents the results of the LBO analysis conducted for each tested geometry. The primary metrics used to evaluate the performance of each design include the volume-averaged temperature within the flame tube and the volume integral of heat release. Additionally, an area-weighted average of the mixture fraction, calculated at the outlet section, is used to monitor the evolution of the mixing flow field as the inlet boundary conditions change. The results begin with an in-depth

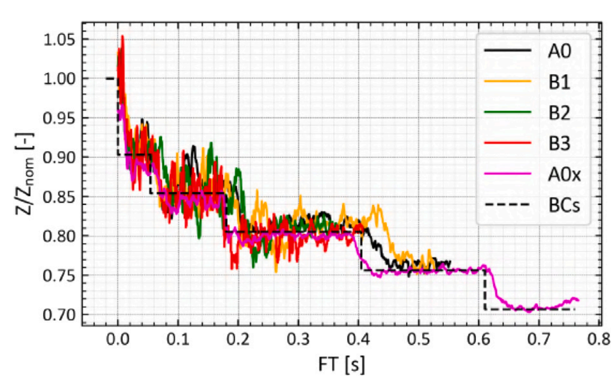

Fig. 11. Area-weighted averaged normalised mixture fraction plots as a function of the flow time for each simulated geometry. Dashed lines indicate the nominal mixture fraction corresponding to each phase of fuel mass flow rate reduction.

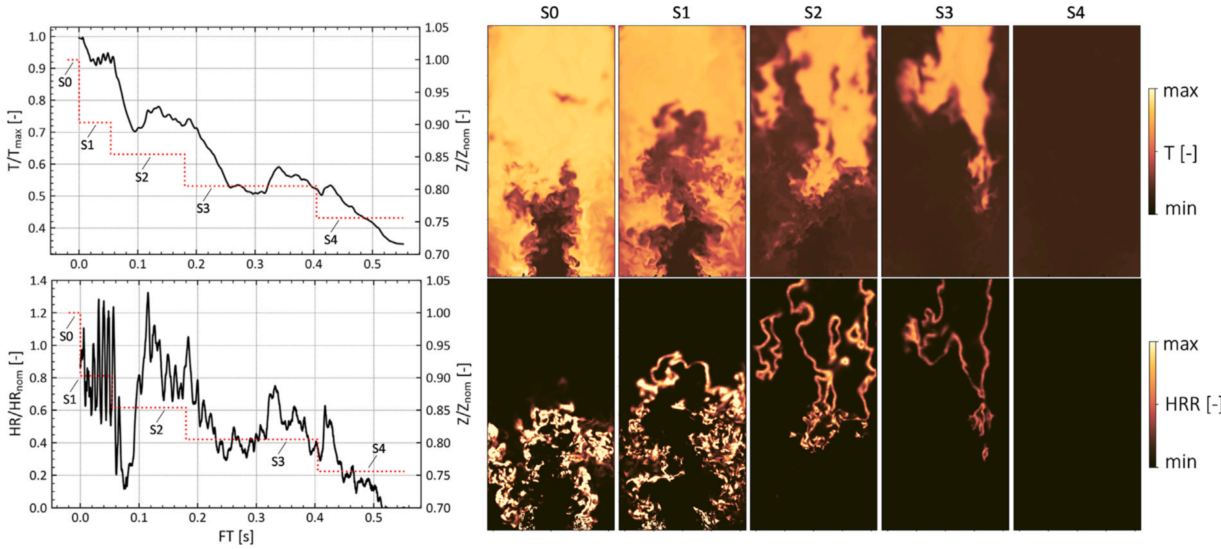

Fig. 12. Left: normalised volume-averaged temperature and volume integral of heat release plots; the red dashed line illustrates the normalised nominal mixture fraction corresponding to each change in boundary conditions. Right: static temperature and heat release rate contours on the midplane section of the burner at the end of each fuel mass flow rate drop.

analysis of LBO dynamics for the baseline geometry (A0). Next, the impact of an alternative fuel injection strategy in the premixing duct is assessed, followed by a brief evaluation of the effects of the pilot line design. Finally, the two proposed swirler designs are compared using similar criteria.

Fig. 11 displays the area-weighted average mixture fraction plots computed on a cross-sectional plane in the downstream region of the flame tube, illustrating the fuel drop steps applied to each geometry. Similar flow times were employed for each geometry during corresponding steps to facilitate visual comparison, as shown in Fig. 11. Minor variations arise based on the timing of flame stabilisation occurrence. Each LBO simulation required a total flow time of approximately 0.55 s from the stabilised starting operating point conditions, except for the corotating swirler solution, which took almost 0.8 s to reach blow-out. Considering an estimated flow-through-time (FTT) of about 0.014 s, this corresponds to approximately 40 FTTs. The dashed line indicates the steps for the applied boundary condition. When reducing the fuel mass flow rate, it takes approximately 2.5 FTTs to uniformly fill the chamber with the new mixture. This process involves the convective transport of the new information from the inlet across the burner, followed by a mixing phase where the old and new boundary conditions interact until the new conditions are fully established. This dynamic further underscores the computational cost associated with each LBO simulation.

6.1. Baseline LBO dynamics

As previously mentioned, step "zero" of the LBO analysis entails simulating the selected geometry under the specified starting test point operating conditions. This initial test point was first applied to the baseline geometry (A0) to validate the numerical setup used throughout this work. Detailed information on the validation process is not included here for brevity, and readers are encouraged to consult [29,30] for comprehensive insights.

Starting from the stabilised solution of the reference operating condition (S0), the LBO numerical procedure, as previously described, proceeds through a series of progressive fuel mass flow rate reductions. The initial step applies a 10% reduction in the inlet mixture's equivalence ratio. Following a delay of approximately 7–10 ms – corresponding to the flow-through time of the chamber – the flame exhibits an immediate response, characterised by decreases in both heat release and temperature. These values stabilise at around 90% of their nominal levels. During this phase, the flame appears elongated, as illustrated in the contour maps of Fig. 12. Notably, the temperature at the pilot exit is significantly reduced, coinciding with small local extinction events that occur near the regions of higher local strain values. However, the flame retains a stable pilot-anchored configuration for approximately 60 ms until the second reduction in fuel mass flow rate is applied, which corresponds to a further 5% decrease in the equivalence ratio. At this stage, the flame experiences a drastic temperature drop that stabilises after around 50 ms, while heat release displays severe fluctuations. During this transient phase, the flame, as depicted in the heat release maps, is progressively quenched, ultimately adopting a new lifted configuration approximately 50 mm from the dome. Despite this, the flame is capable of periodically reaching the pilots' downstream region, resulting in "stable" near-blow-out flame dynamics. After a total simulation time of 0.18 s, another 5% reduction in the inlet equivalence ratio is applied. This results in another sharp decrease in both temperature and heat release, leading to an even more lifted flame configuration. The highest temperature region becomes predominantly located within the downstream flame tube, yet the flame continues to exhibit the dynamics observed in the previous phase, intermittently reaching the downstream region of the pilots. Finally, upon applying the fourth reduction in fuel mass flow rate, the flame encounters a complete blow-out. The described blow-off dynamic is characterised by a spiral vortex structure with a frequency of 40 Hz, whereby the flame transitions from a stable anchored configuration to being progressively ejected, as depicted in Fig. 13, where the flame topology evolution over one period of the frequency mentioned above is displayed. For a more comprehensive understanding of the flame dynamics involved in the LBO process, Fig. 14 presents scatter plots of temperature and stretch as a function of the mixture fraction. Under the initial operating conditions (S0) and after the first fuel mass flow rate reduction (S1), combustion occurs across a broad range of equivalence ratios, reflecting a flame anchored to the locally diffusive pilot flames, primarily located in the upstream section of the chamber, where the mixing process remains incomplete. The flame also demonstrates high resistance to strain, with high-temperature spots occurring at elevated stretch values, predominantly associated with a rich mixture, further indicating a flame anchored to the pilots operating under a locally diffusive regime. In contrast, the temperature distributions for the second and third fuel reductions exhibit sharp peaks concentrated around the nominal mixture fraction values of each phase, indicating a heavily lifted flame, with the highest temperature regions confined to the downstream

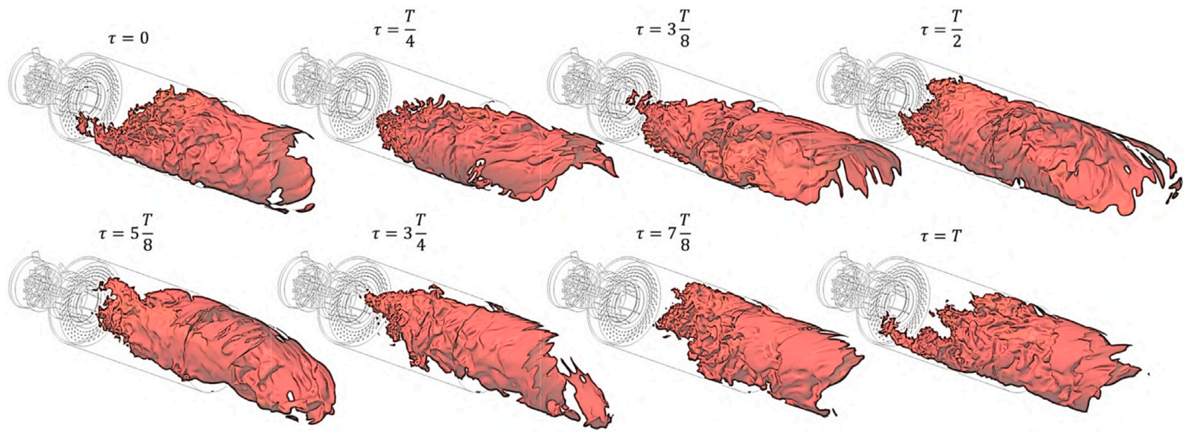

Fig. 13. Flame dynamics over one period of the observed 40 Hz frequency for 15% (S2) fuel mass flow rate reduction. The flame front is identified by the iso-surface of Progress Variable at 0.5.

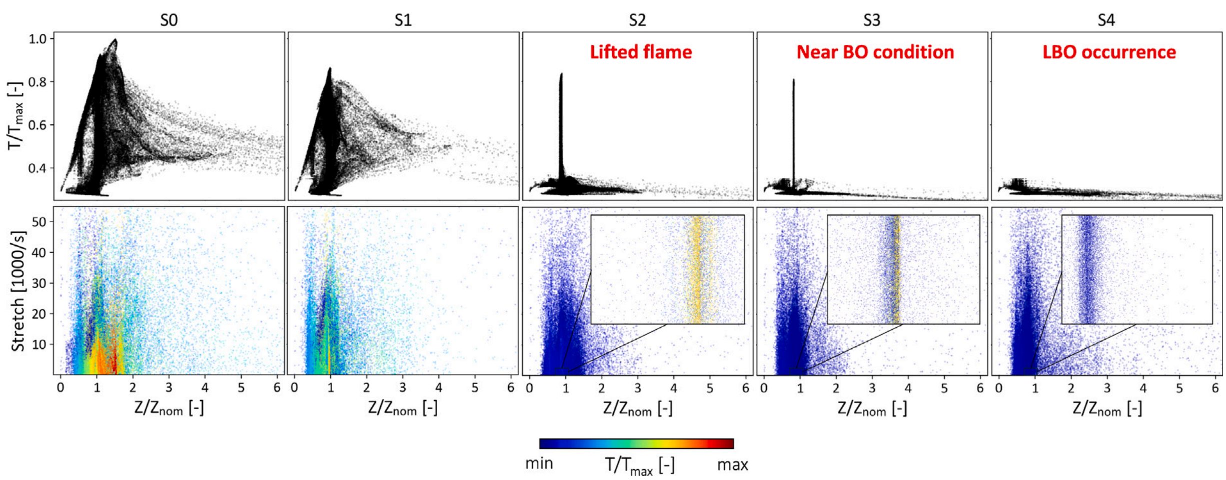

Fig. 14. Scatter plots for the reference plane of the domain. Temperature (top) and Stretch (bottom) as a function of the mixture fraction at the end of each fuel mass flow rate reduction phase. In the stretch graphs, the scatter points are coloured by the temperature.

portion of the flame tube, where the mixing process is fully completed. This trend is further supported by the stretch scatter plots, which show high temperatures occurring only at low stretch values, characteristic of the flow stabilising after the mixing process concludes and becoming largely undisturbed. Finally, after the last fuel mass flow rate reduction, the onset of LBO is observed.

Importantly, to assess the statistical steadiness of the third phase (S3), a time-averaging procedure was applied to the monitored quantities. Specifically, averaging was activated once the instantaneous signals, after an initial transient decay due to the change in boundary conditions, began oscillating around a seemingly constant mean value. Since these mean values remained effectively unchanged for over 200 ms (approximately 15 FTTs), the phase was considered sufficiently settled for analysis, despite the presence of strong fluctuations.

It is worth noting that a formal criterion for the completion of extinction has been assumed to occur when the volume-averaged temperature within the entire flame tube reaches the mixture inlet temperature. Alternative definitions available in the literature, such as that proposed by Cavaliere et al. [80], consider the blow-out event complete when the OH* chemiluminescence total emission falls below 10% of its mean value prior to decay. In this context, a similar approach can be applied to the heat-release rate value approximately.

6.2. Premixing duct design: LBO analysis

A second LBO analysis was conducted on an alternative premixer featuring fuel injection at the tip of the outer swirler (B1). As shown

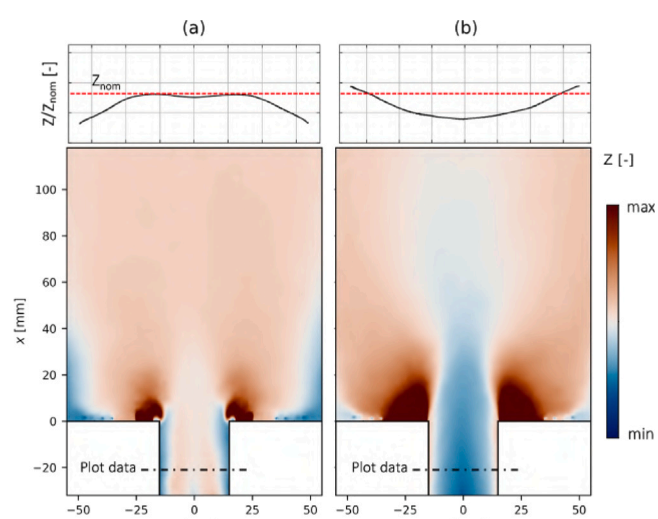

Fig. 15. Mixture fraction contours on the midplane of the burner for the external (a) and internal (b) swirler fuel injection configurations, i.e., A0 and B1, respectively. The inner swirler injection ensures the delivery of a highly premixed mixture within the primary zone, while the outer swirler, coupled with a conical-shaped premixing duct, enriches the pilot region, thus enhancing local flame stabilisation. Design details omitted.

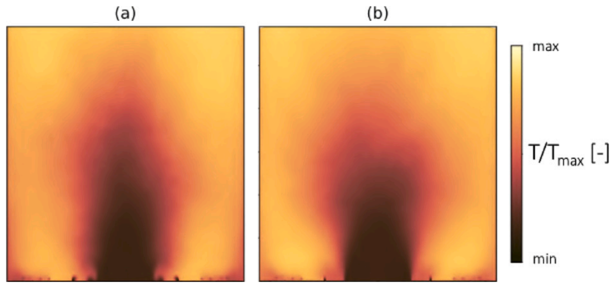

Fig. 16. Time-averaged temperature contours on the midplane of the burner for the A0 (a) and B1 (b) configurations.

in Fig. 15b, this configuration forces the fuel to concentrate near the conical wall of the duct, creating significant enrichment in the pilots' region upon entering the chamber, at the expense of a substantially leaner mixture within the primary zone's central region. While this setup is intended to improve flame stabilisation, it is essential to emphasise that it is viable only in EGR applications. Under standard air conditions, it would result in a substantial increase in NO_x emissions due to elevated local temperatures [81].

The effect of adopting a different fuel injection strategy within the premixer is evident even under the starting test point operating conditions. Fig. 16 illustrates the time-averaged normalised temperature fields for the inner (a) and outer (b) swirler fuel injection configurations. The A0 configuration exhibits a noticeably longer flame than the B1 geometry, suggesting higher reactivity associated with the latter. Additionally, as anticipated from the mixing field, the pilot region displays locally elevated temperatures, which support flame anchoring near blow-out conditions, as will be further detailed. Moving to the LBO, Fig. 17 illustrates the volume-averaged normalised temperature plots as a function of flow time for both premixer configurations. The two design solutions exhibit similar performance during the initial fuel mass flow rate drop (S1), but a 15% reduction (S2) reveals higher temperatures for the B1 configuration compared to A0. During this phase, B1 maintains a stable pilot-anchored flame, whereas A0 displays a heavily lifted and elongated flame, as shown in Fig. 18, which presents instantaneous temperature fields on the midplane of the burner for A0 and B1 at each fuel reduction step. A clearer visualisation of the flame shapes is provided in Fig. 19, which displays iso-surfaces of the progress variable at 0.5, coloured by temperature, for both A0 and B1 geometries at the initial condition (S0) and after a 15% reduction in fuel mass flow rate (S2). A trend reversal occurs with a 20% reduction in fuel mass flow rate (S3), where B1 experiences a sharp temperature

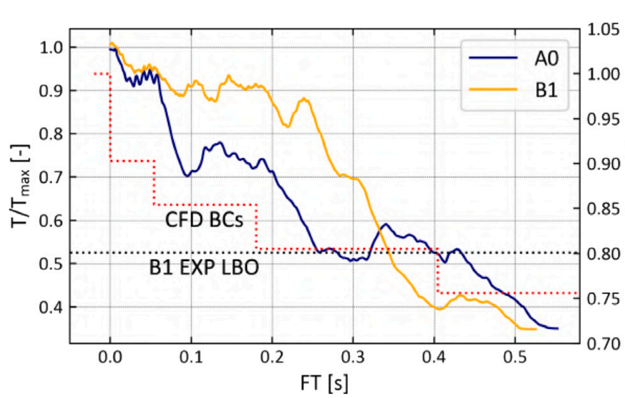

Fig. 17. Volume-averaged normalised temperature over flow time for the A0 and B1 design configurations. The red dotted line depicts the time evolution of the numerical boundary conditions, while the horizontal line marks the experimental extinction point for the B1 configuration, both presented in terms of the normalised mixture fraction.

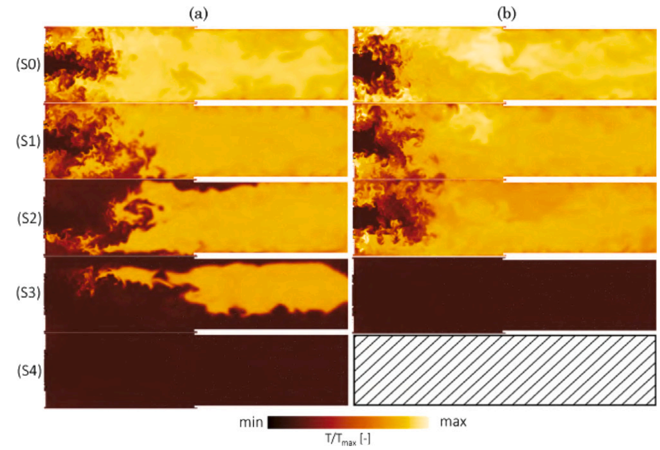

Fig. 18. Instantaneous temperature contours on the midplane of the burner for the A0 (a) and B1 (b) design solutions at the end of each fuel reduction step.

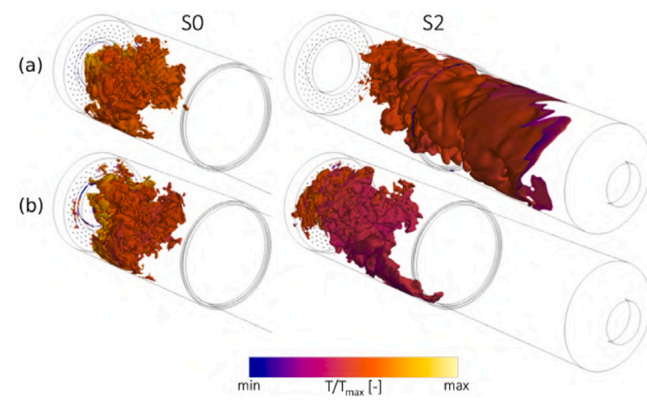

Fig. 19. Iso-surface of Progress Variable = 0.5 coloured by temperature for A0 (a) and B1 (b) geometries under 0% (S0) and 15% (S2) fuel mass flow rate reduction.

drop, with flames transitioning from a stable pilot-anchored position to a heavily lifted state, eventually resulting in a rapid blowout. In contrast, the flame in the A0 configuration, as previously observed, periodically stabilises near the pilots' downstream region, leading to "stable" near-blow-out dynamics and maintaining higher temperatures inside the flame tube compared to B1. With the fourth (−25%) fuel mass flow rate reduction, the A0 flame also undergoes lean blow-out.

An LBO experimental campaign for the B1 geometry, conducted by the THT Lab under the same operating conditions as the simulations, was used to determine the fuel mass flow rate at which extinction occurred. Experimentally, blow-out was observed at a 20.4% fuel mass flow rate reduction, which closely aligns with the numerical prediction of LBO at a 20% reduction (Fig. 17), based on the criteria used in this study. However, since discrete fuel mass flow rate reductions were applied, it is plausible that LBO might have occurred between 15% and 20%. If an average of 17.5% is considered, the discrepancy between the experimental and numerical results narrows down to around 2.9 percentage points (or 14.2%). However, the approach effectively reproduced both the experimental LBO dynamics and the fuel mass flow rate value corresponding to the extinction event, demonstrating the robustness of the predictive model.

A visual summary of flame dynamics during the lean blowout (LBO) process is shown in Fig. 20, which presents time-resolved contours of the heat release rate integrated along the vertical (y) direction. This line integral provides a spatial–temporal projection of the flame structure on the combustor's central axis, offering a clear depiction of axial evolution, including lift-off and retreat behaviour as blowout is approached.

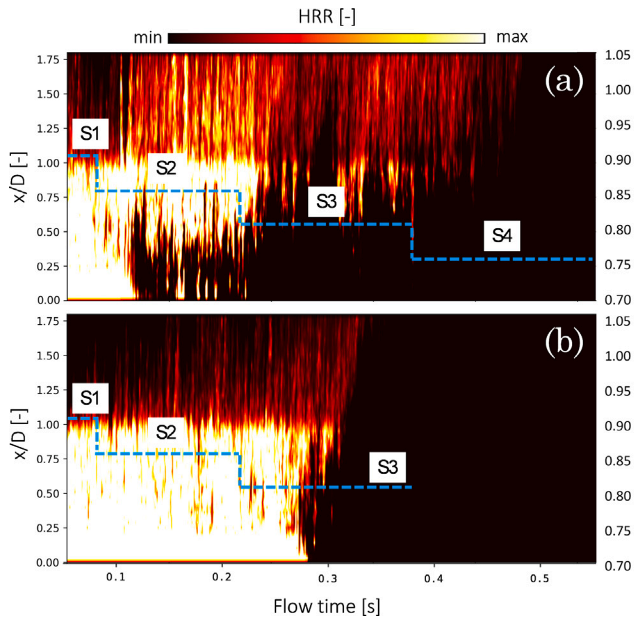

Fig. 20. Time-space evolution contour of Heat Release Rate computed on the midplane section of the burner and projected onto its centreline. A comparison between A0 (a) and B1 (b) design solutions.

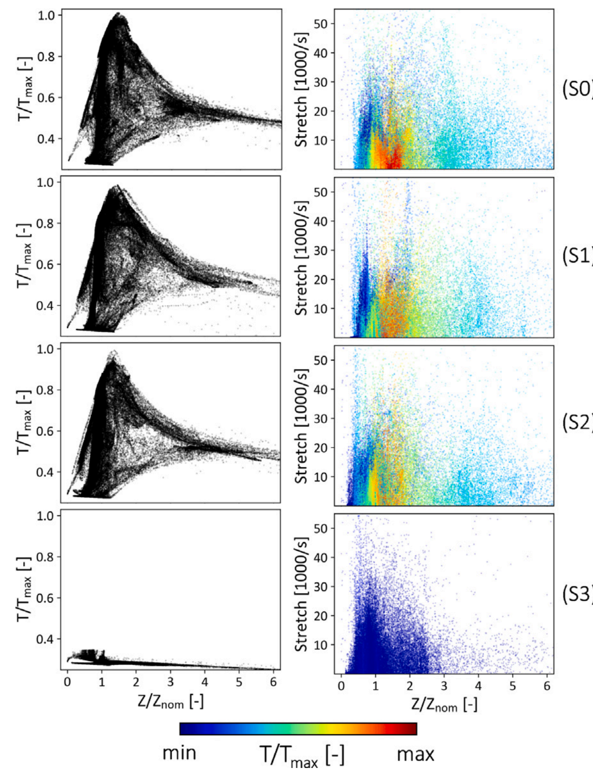

Fig. 21. Scatter plots from the midplane of the burner for the B1 design solution. Temperature (top) and Stretch (bottom) as a function of the mixture fraction at the end of each fuel mass flow rate reduction phase. In the stretch graphs, the scatter points are coloured by the temperature.

Both geometries exhibit flame elongation as the fuel mass flow decreases. However, the outer fuel injection solution (B1) shows greater resistance to flame lift-off during the initial fuel drops (S1–S2), with flames remaining anchored to the pilots and high temperatures maintained near the dome. A significant decline in flame stability occurs thereafter, suddenly transitioning to heavily lifted states and ultimately leading to rapid blow-out (Fig. 20b). By contrast, A0 demonstrates a more linear response to fuel mass flow reduction, maintaining stable near-blow-out dynamics during the S3 condition, thus indicating a wider operability range overall (Fig. 20a).

The differences in flame dynamics between A0 and B1 are clearly evident when comparing the scatter plots in Figs. 14 and 21. Starting from similar distributions, B1, during steps 1 and 2, maintains high temperatures across a wide range of both mixture fraction and stretch values, with a slight progressive concentration on the lean side. This broad mixture fraction distribution highlights the presence of a stable pilot-anchored flame in the upstream region, where the mixing process is still ongoing. Additionally, the flame demonstrates greater resistance to the local high-strain values generated around the pilots. However, despite this enhanced stability, the flame ultimately undergoes a rapid blow-out when the final fuel mass flow rate reduction is applied.

The distinct flame dynamics between A0 and B1 can be attributed to the differences in mixture fraction distributions within the primary zone and around the pilots, as shown in Fig. 15. As discussed, fuel injection at the tip of the outer swirler in B1, combined with a conical-shaped premixer duct, produces a stoichiometric mixture that remains stably concentrated near the dome, enriching the ORZ and supporting an attached flame configuration. However, this local enrichment results in a significantly leaner mixture in the primary zone's central region compared to the baseline design, which instead achieves more uniform mixing prior to entering the chamber, enhancing fuel diffusion in the primary zone. Consequently, while B1 promotes a strongly attached flame even under very lean inlet conditions, a slight flame lift-off can lead to sudden blow-out due to insufficient rich mixture downstream. Conversely, A0's richer downstream mixture can sustain combustion under heavily lifted flame states.

It is important to note that greater resistance to lean blow-out does not inherently signify the optimal design for this application. Reaction completion, particularly regarding CO emissions, is also critical. Given the burner's purpose of accommodating high EGR levels to maximise CO_2 content at the turbine outlet, elevated CO emissions in A0 during S2, attributed to lifted flame dynamics, might make the B1 design a more favourable option.

6.3. Pilot line design: LBO analysis

Given the critical role played by the pilots in the B1 configuration, the inner swirler fuel injection design has been selected to evaluate the impact of different pilot line configurations on the overall flame stability.

From an analysis of the mixing field within the chamber (Fig. 22) for the A0 configuration, no significant effects are attributable to the two

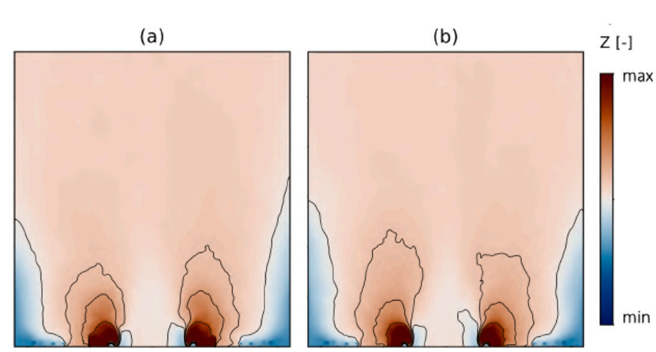

Fig. 22. Mixture fraction contours on the midplane of the chamber for the inward (a) and the outward (b) pilot configurations.

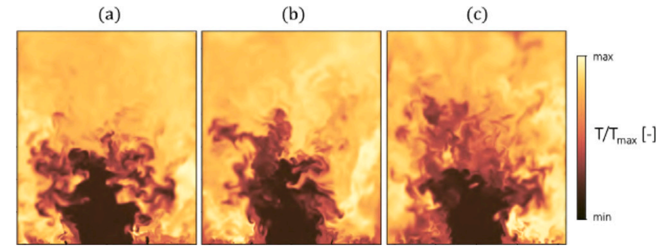

Fig. 23. Normalised instantaneous temperature fields on the midplane of the burner for each simulated pilot line design solution at stable conditions for the starting operating test point: B1 (a), B2 (b), B3 (c).

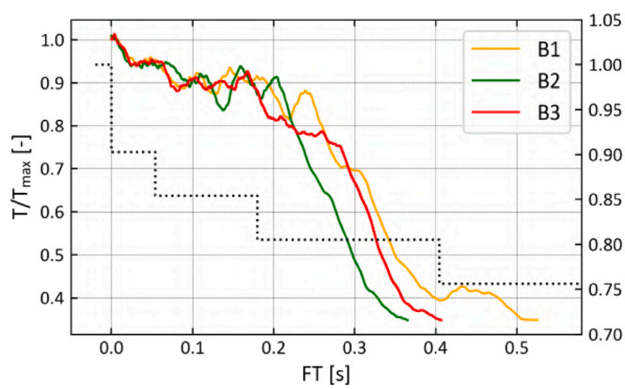

Fig. 24. Volume-averaged normalised temperature as a function of flow time for the three pilot design configurations.

inward-directed pilots, as the flow field is primarily shaped by the premixer design. Consequently, this non-axisymmetric pilot configuration has been excluded from further analyses in this section.

Fig. 23 illustrates the normalised instantaneous temperature fields for each pilot line configuration as observed from the stabilised LES simulations. While B1 and B2 exhibit similar thermal distributions, B3 shows a widespread presence of low-temperature regions. This is attributed to local stoichiometric mixture-wall interactions that reduce the mixture's temperature. Such behaviour arises from the stronger tangential component in the pilot fuel jets of B3, causing them to interact more directly with the dome walls upon entering the chamber.

Proceeding to the LBO analysis, all three configurations demonstrated a similar response to decreasing inlet equivalence ratio: a highly stable flame persisted through the initial two fuel mass flow rate reductions, with a sudden blow-out occurring at step 3 (Fig. 24). In this regard, further distinctions could potentially emerge by reducing the fuel mass flow rate drop between steps 2 and 3. However, as previously noted, the flow field is primarily governed by the premixer geometry and fuel injection strategy, making the pilot line design comparatively less impactful.

Finally, to distinguish between these pilot configurations, an experimental assessment of CO emissions was conducted, as the FGM model does not reliably predict absolute CO levels. Experimentally, the B2 design exhibited the lowest CO emissions under the reference stable operating conditions, suggesting it may be the most favourable pilot line configuration among those tested.

6.4. Swirler design: LBO analysis

The adoption of a co-rotating swirler (A0x), while maintaining the same injection strategy and premixing duct geometry as the baseline (A0), leads to a very different flow field and mixing process within the burner, thus resulting in a conceptually opposite aerothermal field within the chamber, with the classic V-shape jets coupled with a large

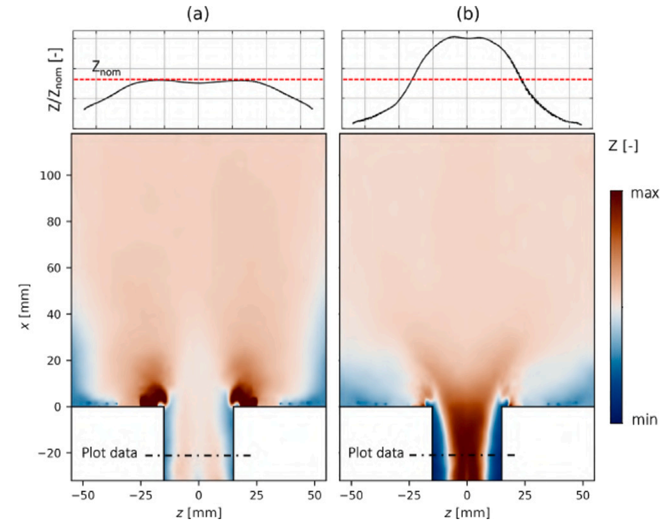

Fig. 25. Mixture fraction contours on the midplane of the burner for the counter-rotating (a) and co-rotating (b) swirler configurations, i.e., A0 and A0x, respectively. The counter-rotating swirler ensures the delivery of a highly premixed mixture within the primary zone; conversely, the co-rotating swirler leads to a locally rich mixture.

inner recirculating zone (IRZ) and two smaller but well-defined outer recirculating zones (ORZ), as previously depicted in Fig. 10. Focusing on the LBO analysis, the flame dynamics leading to extinction are well captured in Fig. 26, which presents the static temperature and heat release rate contours on the midplane section of the burner at the end of each fuel mass flow rate reduction. Unlike the previous pilot-stabilised flames, the co-rotating swirler configuration shows minimal variation in the flame anchoring position despite the progressive reduction in the inlet equivalence ratio. This can be attributed to two key factors: firstly, the swirl-stabilised design inherently promotes flame stabilisation through hot gas recirculation, which pre-heats the reactants, enhancing flame stability. Secondly, the mixture within the burner exhibits a high degree of non-uniformity due to the reduced mixing intensity introduced by the co-rotating swirler. This leads to the consistent delivery of a rich mixture into the primary zone, regardless of the progressive reduction in the nominal equivalence ratio throughout the LBO analysis (Fig. 25).

This behaviour is further corroborated by the temperature scatter plot in Fig. 27, where the temperature peak remains concentrated around the same mixture fraction value, irrespective of the progressively leaner nominal equivalence ratio. The narrow range of mixture fraction values surrounding the nominal value suggests that the flame develops in a region where mixing is nearly complete. Consequently, the flame does not progressively lift; instead, it narrows its spreading angle until blow-off occurs, following a linear trend as the inlet mixture becomes leaner. As the flame anchoring position remains largely unchanged throughout the LBO analysis, the highest temperature values consistently occur around the same strain values, even though the global temperature decreases due to the reduced equivalence ratio and the diminishing flame resistance to stretch, the latter ultimately leading to local flame quenching in the proximity of the shear layers where the flame stabilises.

Comparing this design, identified as A0x, to the previously presented pilot-stabilised solutions, the co-rotating swirler demonstrates the greatest resistance to blow-off, reaching complete flame extinction later than the other configurations, as shown in Fig. 28. It is important to note, however, that due to the specific aerothermal characteristics of a swirl-stabilised design, the volume-averaged temperature inside the combustion chamber is lower than that of the pilot-stabilised designs at each fuel mass flow rate reduction. Therefore, the volume-averaged temperature cannot be directly used to compare combustion efficiency between A0x and the other design solutions.

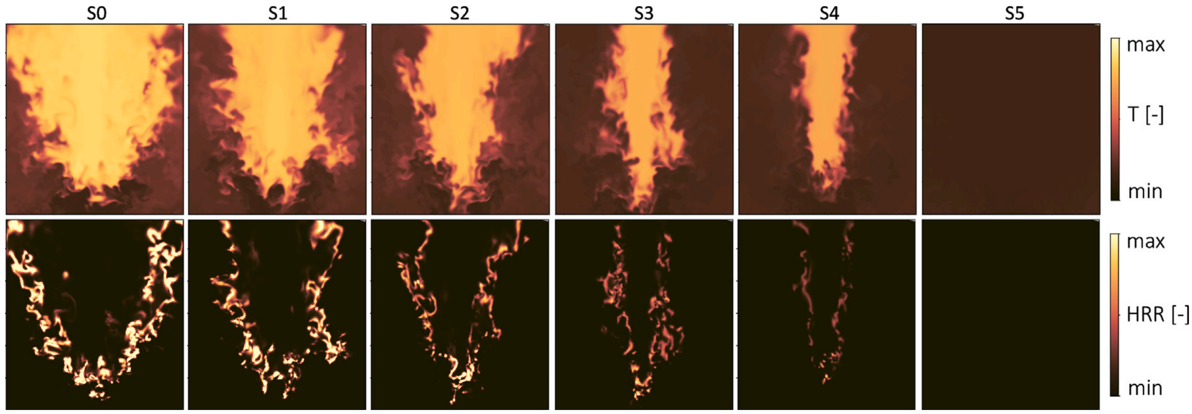

Fig. 26. Instantaneous static temperature and heat release rate contours on the midplane section of the burner at the end of each fuel mass flow rate drop for the A0x burner.

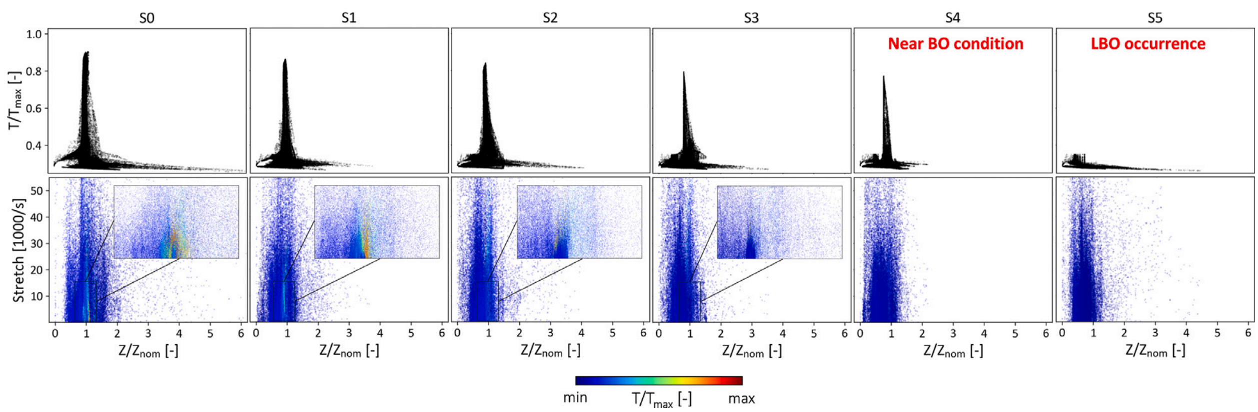

Fig. 27. Scatter plots from the midplane of the burner for the co-rotating swirler. Temperature (top) and Stretch (bottom) as a function of the mixture fraction at the end of each fuel mass flow rate reduction phase. In the stretch graphs, the scatter points are coloured by the temperature.

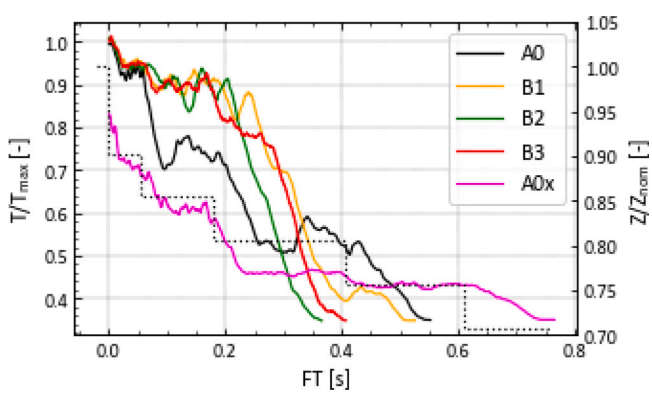

Fig. 28. Volume-averaged normalised temperature plots as a function of flow time for each simulated design solution.

7. Computational costs

All simulations featured in this analysis were executed on an HPC cluster consisting of 20 multicore Intel® Xeon® Gold 6248 CPU nodes. The total computational cost for each simulation, encompassing an initial RANS calculation to establish a starting solution for the LES reference test point, followed by flushing, sampling stages, and the full LBO procedure, was estimated to be approximately 120,000 CPU hours. This results in a cumulative computational expense of around 600,000 CPU hours for the entire comparative analysis.

8. Conclusions

This study explored the impact of burner geometry on flame stability under high CO_2 dilution conditions, leveraging LES-based LBO numerical analysis. Conducted within the framework of the European-funded TRANSITION project, the research aimed to identify burner designs capable of stable operation at elevated EGR levels. Numerical assessments were performed across various burner configurations, involving modifications to the premixer, pilot, and swirler designs, with fuel mass flow rate systematically reduced to simulate LBO conditions.

The key findings of this numerical investigation are summarised below:

- In the baseline configuration (A0), blow-off occurs through the development of a spiral vortex structure oscillating near 40 Hz, leading to a linear transition from a firmly anchored flame operating under partially premixed conditions to a progressively lifted and extinguished state. This finding is significant, as such dynamics were not discernible from experimental data due to the absence of detailed 3D flow visualisation, highlighting the unique insights provided by the CFD analysis.
- Enhanced piloted flame stability was achieved with an alternative premixer design featuring fuel injection at the tip of the outer swirler (B-family configurations). The resulting flame primarily operated in a non-premixed regime and exhibited reduced susceptibility to elongation during the initial LBO phases. However, the presence of a leaner mixture in the primary zone's core region compared to the baseline design led to instability, transitioning to a heavily lifted state and culminating in rapid blow-off.

- The premixer geometry and fuel injection strategy were found to primarily dictate the flow field, rendering the pilot line design relatively less impactful.
- A co-rotating swirler configuration (A0x) was introduced to assess the influence of swirl-stabilisation mechanisms on LBO limits. The consistent delivery of a rich mixture into the primary zone, coupled with the enhanced flame stability associated with hot gas recirculation, led to a different LBO dynamic. The flame, instead of progressively lifting, maintains its anchoring position and narrows its spreading angle until blow-out is reached.
- Among all configurations, the swirl-stabilised flame exhibited the highest blow-out resistance, reaching LBO after a 30% fuel mass flow reduction, while the best-performing pilot-stabilised case (A0) reached LBO at a 25% reduction.
- The FGM model accurately predicted the fuel mass flow rate corresponding to the extinction event measured during the experimental campaign for the B1 configuration.

Ultimately, the final conclusions will rest on experimental validation. Advanced testing at DLR (Deutsches Zentrum für Luft- und Raumfahrt), the German aerospace research centre, will involve configurations A0, B2, and A0x to facilitate the selection of an optimal geometry for full-scale turbine installation and provide critical data for further CFD validation.

These results underscore the pivotal role of burner design in overcoming combustion challenges at high EGR levels. From a computational perspective, the FGM model, with appropriate modifications to capture quenching phenomena, has demonstrated a robust balance between accuracy and efficiency in reconstructing complex transient flame dynamics, such as those observed in LBO events. Future developments could incorporate the approach proposed by Meloni et al. [82] to further enhance the model's predictive capabilities for CO and NO_x emissions.

Nomenclature

Acronyms

ATF	Artificially Thickened Flame
CCS	Carbon Capture and Storage
CFD	Computational Fluid Dynamics
DLN	Dry Low NO_x
EGR	Exhaust Gas Recirculation
ES	External Swirler
FGM	Flamelet Generated Manifold
FR	Finite-Rate
FT	Flow Time
FTT	Flow-Through-Time
GT	Gas Turbine
HPC	High-Performance Computing
HTC	Heat Transfer Coefficient
IRZ	Inner Recirculation Zone
IS	Inner Swirler
LBO	Lean Blow-Out
LES	Large Eddy Simulation
LESIQ	LES Index Quality
LPC	Lean Premixed Combustor
ORZ	Outer Recirculation Zone
PDF	Probability Density Function
PISO	Pressure-Implicit with Splitting of Operators
PMX	Premixer
RANS	Reynolds-Averaged Navier–Stokes
THT	Technology for High Temperature
UDF	User Defined Function
WALE	Wall-Adapting Local Eddy-viscosity

Symbols

a	Strain rate [s^{-1}]
c	FGM unnormalised reaction progress variable [–]
k	Turbulent kinetic energy [$m^2\ s^{-2}$]
n	Normal vector to the flame front
P	Static Pressure [Pa]
$P(x)$	PDF of the x-variable
S_l	Laminar flame speed [$m\ s^{-1}$]
u_i	Velocity i-component [$m\ s^{-1}$]
Y_i	Elemental Mass Fraction of the i-species
Z	Mixture fraction

Greek

Γ	Extended-FR correction factor
Γ_k	Extended-FR efficiency function
Δ	LES filter length [–]
δ_{ij}	Kronecker delta
κ	Stretch [s^{-1}]
ρ	Density [$kg\ m^{-3}$]
σ_c	Curvature [s^{-1}]
ψ	Extended-FR heat loss parameter
$\dot{\omega}_c$	Turbulent progress variable source term [s^{-1}]

Subscripts

ad	Adiabatic
b	Burnt gases
eq	Equilibrium
o	Adiabatic unstrained
res	Resolved quantity
sgs	Sub-grid scale modelled quantity
T	Turbulent quantity

Superscripts

$'$	Reynolds fluctuation
$''$	Favre fluctuation
$-$	Reynolds averaged
$\sim$	Favre averaged

CRediT authorship contribution statement

Gianmarco Lemmi: Writing – review & editing, Writing – original draft, Visualization, Validation, Methodology, Investigation, Data curation. **Simone Castellani:** Writing – review & editing, Supervision, Conceptualization. **Roberto Meloni:** Writing – review & editing, Supervision, Resources. **Sofia Galeotti:** Supervision, Resources. **Antonio Andreini:** Writing – review & editing, Supervision, Project administration, Funding acquisition, Conceptualization.

Declaration of competing interest

The authors declare the following financial interests/personal relationships which may be considered as potential competing interests: Antonio Andreini reports financial support was provided by Horizon Europe. If there are other authors, they declare that they have no known competing financial interests or personal relationships that could have appeared to influence the work reported in this paper.

Acknowledgements

The present research activity was carried out in the framework of TRANSITION (fuTure hydRogen Assisted gas turbiNeS for effective carbon capTure IntegratiON). This project has received funding from the Europen Union's Horizon Europe research and Innovation programme under Grant Agreement No 101069665. The Authors gratefully acknowledge this financial support.

Funded by the European Union

Data availability

Data will be made available on request.

References

[1] Tsiropoulos I, Nijs W, Tarvydas D, Castello PR. Towards net-zero emissions in the EU energy system by 2050 – insights from scenarios in line with the 2030 and 2050 ambitions of the European green deal. In: EUR 29981 EN. Publications Office of the European Union; 2020, http://dx.doi.org/10.2760/081488.

[2] UNFCCC. Paris agreement. United Nations; 2015.

[3] Ritchie H, Rosado P, Roser M. CO2 emissions by fuel. Our World Data 2020. https://ourworldindata.org/emissions-by-fuel.

[4] Gonzalez-Salazar MA, Kirsten T, Prchlik L. Review of the operational flexibility and emissions of gas- and coal-fired power plants in a future with growing renewables. Renew Sustain Energy Rev 2018;82:1497–513. http://dx.doi.org/10.1016/j.rser.2017.05.278.

[5] Öberg S, Odenberger M, Johnsson F. Exploring the competitiveness of hydrogen-fueled gas turbines in future energy systems. Int J Hydrog Energy 2021;47:624–44. http://dx.doi.org/10.1016/j.ijhydene.2021.10.035.

[6] Rasul M, Hazrat M, Sattar M, Jahirul M, Shearer M. The future of hydrogen: Challenges on production, storage and applications. Energy Convers Manage 2022;272:116326. http://dx.doi.org/10.1016/j.enconman.2022.116326.

[7] Abdin Z, Zafaranloo A, Rafiee A, Mérida W, Lipinski W, Khalilpour KR. Hydrogen as an energy vector. Renew Sustain Energy Rev 2020;120:109620. http://dx.doi.org/10.1016/j.rser.2019.109620.

[8] Ahmed SF, Mofijur M, Nuzhat S, Rafa N, Musharrat A, Lam SS, Boretti A. Sustainable hydrogen production: Technological advancements and economic analysis. Int J Hydrog Energy 2022;47(88):37227–55. http://dx.doi.org/10.1016/j.ijhydene.2021.12.029, Hydrogen Energy Technology for Future.

[9] Abdalla AM, Hossain S, Nisfindy OB, Azad AT, Dawood M, Azad AK. Hydrogen production, storage, transportation and key challenges with applications: A review. Energy Convers Manage 2018;165:602–27. http://dx.doi.org/10.1016/j.enconman.2018.03.088.

[10] Boot-Handford M, Abanades J, Anthony E, Blunt M, Brandani S, Mac Dowell N, Andez J, et al. Carbon capture and storage update. Energy Environ Sci 2014;7:130–89. http://dx.doi.org/10.1039/c3ee42350f.

[11] Popa A, Edwards R, Aandi I. Carbon capture considerations for combined cycle gas turbine. Energy Procedia 2011;4:2315–23. http://dx.doi.org/10.1016/j.egypro.2011.02.122, 10th International Conference on Greenhouse Gas Control Technologies.

[12] Røkke PE, Hustad JE. Exhaust gas recirculation in gas turbines for reduction of CO2 emissions; combustion testing with focus on stability and emissions. Int J Thermodyn 2005;8:167–73. http://dx.doi.org/10.5541/ijot.158.

[13] Herraiz L, Diego M, Bellas J-M, Finney K, Pourkashanian M, Runyon J, Giles A, Marsh R, Lucquiaud M. Selective exhaust gas recycling in gas turbines with CO2 capture: A comprehensive technology assessment. SSRN Electron J 2021;16. http://dx.doi.org/10.2139/ssrn.3811445.

[14] Tanaka Y, Nose M, Nakao MT, Saitoh K, Ito E. Development of low NOx combustion system with EGR for 1700°C-class gas turbine. In: Mitsubishi heavy industries technical review. 50, 2013, p. 1–6, URL: https://api.semanticscholar.org/CorpusID:55369324.

[15] Burnes D, Saxena P, Dunn P. Study of Using Exhaust Gas Recirculation on a Gas Turbine for Carbon Capture. In: Proceedings of the ASME turbo expo 2020: turbomachinery technical conference and exposition. Turbo expo: power for land, sea, and air, 5: Controls, Diagnostics, and Instrumentation; Cycle Innovations; Cycle Innovations: Energy Storage, 2020, V005T06A034. http://dx.doi.org/10.1115/GT2020-16080.

[16] Li H, Zhou X, Jeffries JB, Hanson RK. Active control of lean blowout in a swirl-stabilized combustor using a tunable diode laser. Proc Combust Inst 2007;31(2):3215–23. http://dx.doi.org/10.1016/j.proci.2006.07.006.

[17] ElKady AM, Evulet A, Brand A, Ursin TP, Lynghjem A. Exhaust Gas Recirculation in DLN F-Class Gas Turbines for Post-Combustion CO2 Capture. In: Proceedings of the ASME turbo expo 2008: turbomachinery technical conference and exposition. Turbo expo: power for land, sea, and air, 3: Combustion, Fuels and Emissions, Parts A and B, 2008, p. 847–54. http://dx.doi.org/10.1115/GT2008-51152.

[18] Xie M, Fu J, Zhang Y, Shu J, Ma Y, Liu J, Zeng D. Numerical analysis on the effects of CO2 dilution on the laminar burning velocity of premixed methane/air flame with elevated initial temperature and pressure. Fuel 2020;264(December 2019):116858. http://dx.doi.org/10.1016/j.fuel.2019.116858.

[19] Chan YL, Zhu MM, Zhang ZZ, Liu PF, Zhang DK. The Effect of CO2 Dilution on the Laminar Burning Velocity of Premixed Methane/Air Flames. Energy Procedia 2015;75:3048–53. http://dx.doi.org/10.1016/j.egypro.2015.07.621.

[20] De Persis S, Cabot G, Pillier L, Gökalp I, Boukhalfa AM. Study of lean premixed methane combustion with CO2 dilution under gas turbine conditions. Energy Fuels 2013;27(2):1093–103. http://dx.doi.org/10.1021/ef3016365.

[21] Evulet AT, ELKady AM, Branda AR, Chinn D. On the performance and operability of GE's dry low NOx combustors utilizing exhaust gas recirculation for PostCombustion carbon capture. Energy Procedia 2009;1(1):3809–16. http://dx.doi.org/10.1016/j.egypro.2009.02.182, Greenhouse Gas Control Technologies 9.

[22] Burdet A, Lachaux T, de la Cruz Garcia M, Winkler D. Combustion Under Flue Gas Recirculation Conditions in a Gas Turbine Lean Premix Burner. In: Proceedings of the ASME turbo expo 2010: turbomachinery technical conference and exposition. Turbo expo: power for land, sea, and air, vol. 2: Combustion, Fuels and Emissions, Parts A and B, 2010, p. 1083–91. http://dx.doi.org/10.1115/GT2010-23396.

[23] Guethe F, Stankovic D, Genin F, Syed K, Winkler D. Flue Gas Recirculation of the Alstom Sequential Gas Turbine Combustor Tested at High Pressure. In: Proceedings of the ASME turbo expo 2011: turbomachinery technical conference and exposition. Turbo expo: power for land, sea, and air, vol. 2: Combustion, Fuels and Emissions, Parts A and B, 2011, p. 399–408. http://dx.doi.org/10.1115/GT2011-45379.

[24] Liu C, Chen G, Sipöcz N, Assadi M, Bai X. Characteristics of oxy-fuel combustion in gas turbines. Appl Energy 2012;89(1):387–94. http://dx.doi.org/10.1016/j.apenergy.2011.08.004, Special issue on Thermal Energy Management in the Process Industries.

[25] Kvamsdal HM, Jordal K, Bolland O. A quantitative comparison of gas turbine cycles with CO2 capture. Energy 2007;32(1):10–24. http://dx.doi.org/10.1016/j.energy.2006.02.006.

[26] Bolland O, Mathieu P. Comparison of two CO2 removal options in combined cycle power plants. Energy Convers Manage 1998;39(16):1653–63. http://dx.doi.org/10.1016/S0196-8904(98)00078-8.

[27] Dillon D, Panesar R, Wall R, Allam R, White V, Gibbins J, Haines M. Oxy-combustion processes for CO2 capture from advanced supercritical pf and NGCC power plant. In: Rubin E, Keith D, Gilboy C, Wilson M, Morris T, Gale J, Thambimuthu K, editors. Greenhouse gas control technologies 7. Oxford: Elsevier Science Ltd; 2005, p. 211–20. http://dx.doi.org/10.1016/B978-008044704-9/50022-7.

[28] Transition. Future hydrogen assisted gas turbines for effective carbon capture integration. 2022, https://transition-horizon.eu/. [Accessed 5 December 2024].

[29] Lemmi G, Castellani S, Nassini P, Picchi A, Galeotti S, Becchi R, Andreini A, Babazzi G, Meloni R. FGM vs ATF: A comparative LES analysis in predicting the flame characteristics of an industrial lean premixed burner for gas turbine applications. Fuel Commun 2024;19:100117. http://dx.doi.org/10.1016/j.jfueco.2024.100117.

[30] Lemmi G, Castellani S, Galeotti S, Picchi A, Becchi R, Andreini A, Meloni R, Babazzi G. Prediction of the Flame Characteristics of an Industrial Gas Turbine Operated With CO2-Diluted Air Through an LES-Based CFD Analysis: A Comparison Between FGM and ATF. J Eng Gas Turb Power 2024;1–31. http://dx.doi.org/10.1115/1.4066510.

[31] Shanbhogue SJ, Husain S, Lieuwen T. Lean blowoff of bluff body stabilized flames: Scaling and dynamics. Prog Energy Combust Sci 2009;35(1):98–120. http://dx.doi.org/10.1016/j.pecs.2008.07.003.

[32] Plee S, Mellor A. Characteristic time correlation for lean blowoff of bluff-body-stabilized flames. Combust Flame 1979;35:61–80. http://dx.doi.org/10.1016/0010-2180(79)90007-5.

[33] Longwell JP, Frost EE, Weiss MA. Flame stability in bluff body recirculation zones. Ind Eng Chem 1953;45(8):1629–33. http://dx.doi.org/10.1021/ie50524a019.

[34] Williams G, Hottel H, Scurlock A. Flame stabilization and propagation in high velocity gas streams. Symp Combust Flame Explos Phenom 1948;3(1):21–40. http://dx.doi.org/10.1016/S1062-2896(49)80006-7, Third Symposium on Combustion and Flame and Explosion Phenomena.

[35] Kundu KM, Banerjee D, and DB. Theoretical analysis on flame stabilization by a bluff-body. Combust Sci Technol 1977;17(3–4):153–62. http://dx.doi.org/10.1080/00102207708946825.

[36] Zukoski EE. Flame stabilization on bluff bodies at low and intermediate Reynolds numbers (Ph.D. thesis), California Institute of Technology; 1954, URL: https://api.semanticscholar.org/CorpusID:94250026.

[37] Yamaguchi S, Ohiwa N, Hasegawa T. Structure and blow-off mechanism of rod-stabilized premixed flame. Combust Flame 1985;62(1):31–41. http://dx.doi.org/10.1016/0010-2180(85)90091-4.

[38] Pan J, Ballal D. Chemistry and turbulence effects in bluff-body stabilized flames. In: 30th aerospace sciences meeting and exhibit. AIAA; 1992, http://dx.doi.org/10.2514/6.1992-771.

[39] Dawson J, Gordon R, Kariuki J, Mastorakos E, Masri A, Juddoo M. Visualization of blow-off events in bluff-body stabilized turbulent premixed flames. Proc Combust Inst 2011;33(1):1559–66. http://dx.doi.org/10.1016/j.proci.2010.05.044.

[40] Kariuki J, Dawson JR, Mastorakos E. Measurements in turbulent premixed bluff body flames close to blow-off. Combust Flame 2012;159(8):2589–607. http://dx.doi.org/10.1016/j.combustflame.2012.01.005, Special Issue on Turbulent Combustion.

[41] Morales AJ, Lasky IM, Geikie MK, Engelmann CA, Ahmed KA. Mechanisms of flame extinction and lean blowout of bluff body stabilized flames. Combust Flame 2019;203:31–45. http://dx.doi.org/10.1016/j.combustflame.2019.02.002.

[42] Chaudhuri S, Kostka S, Renfro MW, Cetegen BM. Blowoff dynamics of bluff body stabilized turbulent premixed flames. Combust Flame 2010;157(4):790–802. http://dx.doi.org/10.1016/j.combustflame.2009.10.020.

[43] Stöhr M, Boxx I, Carter C, Meier W. Dynamics of lean blowout of a swirl-stabilized flame in a gas turbine model combustor. Proc Combust Inst 2011;33(2):2953–60. http://dx.doi.org/10.1016/j.proci.2010.06.103.

[44] Pignatelli F, Sanned D, Derafshzan S, Szasz R, Bai X, Richter M, Ehn A, Lörstad D, Petersson P, Subash A. Impact of pilot flame and hydrogen enrichment on turbulent methane/hydrogen/air swirling premixed flames in a model gas turbine combustor. Exp Therm Fluid Sci 2024;152:111124. http://dx.doi.org/10.1016/j.expthermflusci.2023.111124.

[45] Zubrilin IA, Gurakov NI, Matveev SG. Lean blowout limit prediction in a combustor with the Pilot flame. Energy Procedia 2017;141:273–81. http://dx.doi.org/10.1016/j.egypro.2017.11.105, Power and Energy Systems Engineering.

[46] Yang J, Zhang K, Liu C, Ruan C, Liu F, Xu G. Investigation of the effect of pilot burner on lean blow out performance of a staged injector. J Therm Sci 2014;23(6):600–8. http://dx.doi.org/10.1007/s11630-014-0747-x.

[47] Avila Jimenez CD, Cardona S, Juaied MA, Younes M, Jamal A, Guiberti TF, Roberts WL. Influence of the pilot flame on the morphology and exhaust emissions of NH3-CH4-air swirl flames using a reduced-scale burner at atmospheric pressure. Energies 2023;16(1). http://dx.doi.org/10.3390/en16010231, URL: https://www.mdpi.com/1996-1073/16/1/231.

[48] Muruganandam T, Seitzman J. Origin of lean blow out precursors in swirled gas turbine combustors. In: 43rd AIAA aerospace sciences meeting and exhibit. 2005, http://dx.doi.org/10.2514/6.2005-1163, URL: https://arc.aiaa.org/doi/abs/10.2514/6.2005-1163.

[49] Guiberti T, Cutcher H, Roberts W, Masri A. Influence of pilot flame parameters on the stability of turbulent jet flames. Energy Fuels 2016;31. http://dx.doi.org/10.1021/acs.energyfuels.6b02052.

[50] Galeotti S, Picchi A, Becchi R, Meloni R, Babazzi G, Romano C, Andreini A. Experimental characterization of an industrial burner operated with simulated EGR. Appl Therm Eng 2024;246:122943. http://dx.doi.org/10.1016/j.applthermaleng.2024.122943.

[51] Cerutti M, Riccio G, Andreini A, Becchi R, Facchini B, Picchi A. Experimental and numerical investigations of novel natural gas low nox burners for heavy duty gas turbine. In: Proceedings of the ASME turbo expo 2018: turbomachinery technical conference and exposition. Turbo expo, vol. 4B: Combustion, Fuels, and Emissions, 2018, V04BT04A031. http://dx.doi.org/10.1115/GT2018-76670.

[52] Ateshkadi A, McDonell VG, Samuelsen G. Lean blowout model for a spray-fired swirl-stabilized combustor. Proc Combust Inst 2000;28(1):1281–8. http://dx.doi.org/10.1016/S0082-0784(00)80341-0.

[53] Johnson M, Littlejohn D, Nazeer W, Smith K, Cheng R. A comparison of the flowfields and emissions of high-swirl injectors and low-swirl injectors for lean premixed gas turbines. Proc Combust Inst 2005;30(2):2867–74. http://dx.doi.org/10.1016/j.proci.2004.07.040.

[54] Kumaran K, Shet U. Effect of swirl on lean flame limits of pilot-stabilized open premixed turbulent flames. Combust Flame 2007;151(1):391–5. http://dx.doi.org/10.1016/j.combustflame.2007.06.016, URL: https://www.sciencedirect.com/science/article/pii/S0010218007001691.

[55] Li H, Elkady AM, Evulet AT. Effect of exhaust gas recirculation on NOx formation in premixed combustion system. In: 47th AIAA aerospace sciences meeting including the new horizons forum and aerospace exposition. 2009, p. AIAA2009–226. http://dx.doi.org/10.2514/6.2009-226.

[56] Nair S, Lieuwen T. Acoustic detection of blowout in premixed flames. J Propuls Power 2005;21(1):32–9. http://dx.doi.org/10.2514/1.5658.

[57] Romano S, Meloni R, Riccio G, Nassini PC, Andreini A. Modeling of natural gas composition effect on low NOx burners operation in heavy duty gas turbine. J Eng Gas Turb Power 2021;143. http://dx.doi.org/10.1115/1.4049819.

[58] Babazzi G, Galeotti S, Picchi A, Becchi R, Cerutti M, Andreini A. Combustion Diagnostics and Emissions Measurements of a Novel Low NOx Burner for Industrial Gas Turbine Operated With CO2 Diluted Methane/Air Mixtures. In: Proceedings of the ASME turbo expo 2023: turbomachinery technical conference and exposition. Turbo expo: power for land, sea, and air, vol. 3A: Combustion, Fuels, and Emissions, 2023, V03AT04A018. http://dx.doi.org/10.1115/GT2023-101261.

[59] Galeotti S, Picchi A, Becchi R, Lemmi G, Meloni R, Babazzi G, Andreini A. Experimental and numerical study of the effect of CO_2/N_2 dilution to simulate EGR in GT combustor. In: 46th meeting of the Italian section of the combustion institute, towards net zero carbon society, book of abstract. 2024, p. 240–5.

[60] Ducros F, Franck N, Poinsot T. Wall-adapting local eddy-viscosity models for simulations in complex geometries. Numer Methods Fluid Dyn VI 1998.

[61] Ben-Nasr O, Hadjadj A, Chaudhuri A, Shadloo M. Assessment of subgrid-scale modeling for large-eddy simulation of a spatially-evolving compressible turbulent boundary layer. Comput & Fluids 2017;151:144–58. http://dx.doi.org/10.1016/j.compfluid.2016.07.004, A special issue in honor of Cecil "Chuck" E. Leith.

[62] Issa R. Solution of the implicitly discretised fluid flow equations by operator-splitting. J Comput Phys 1986;62(1):40–65. http://dx.doi.org/10.1016/0021-9991(86)90099-9.

[63] Issa R, Gosman A, Watkins A. The computation of compressible and incompressible recirculating flows by a non-iterative implicit scheme. J Comput Phys 1986;62(1):66–82. http://dx.doi.org/10.1016/0021-9991(86)90100-2.

[64] ANSYS I. ANSYS fluent theory guide. Southpointe 2600 Ansys Drive Canonsburg, PA 15317; 2022, Available at http://www.ansys.com.

[65] Langone L, Sedlmaier J, Nassini PC, Mazzei L, Harth S, Andreini A. Numerical Modeling of Gaseous Partially Premixed Low-Swirl Lifted Flame at Elevated Pressure. In: Proceedings of the ASME turbo expo 2020: turbomachinery technical conference and exposition. Turbo expo: power for land, sea, and air, vol. 4B: Combustion, Fuels, and Emissions, 2020, V04BT04A068. http://dx.doi.org/10.1115/GT2020-16305.

[66] Peters N. Laminar flamelet concepts in turbulent combustion. Symp (Int) Combust 1988;21(1):1231–50. http://dx.doi.org/10.1016/S0082-0784(88)80355-2, Twenty-First Symposuim (International on Combustion).

[67] Hadadpour A, Xu S, Zhang Y, Bai X-S, Jangi M. An extended FGM model with transported PDF for LES of spray combustion. Proc Combust Inst 2023;39(4):4889–98. http://dx.doi.org/10.1016/j.proci.2022.09.014.

[68] Frenklach M, Wang H, Goldenberg M, Smith G, Golden D, Bowman C, Hanson R, Gardiner W, Lissianski V. GRI-mech—an optimized detailed chemical reaction mechanism for methane combustion. Technical report, Gas Research Institute Chicago; 1995.

[69] Bilger R. Reaction rates in diffusion flames. Combust Flame 1977;30:277–84. http://dx.doi.org/10.1016/0010-2180(77)90076-1.

[70] van Oijen J, Goey P. Modelling of premixed laminar flames using flamelet-generated manifolds. Combust Sci Technol 2000;161:113–37. http://dx.doi.org/10.1080/00102200008935814.

[71] Ramaekers W, Albrecht BA, van Oijen J, de Goey LPH. The application of flamelet generated manifolds in modelling of turbulent partially-premixed flames. In: Proceedings of the fluent benelux user group meeting. 1990, p. 3D, URL: https://api.semanticscholar.org/CorpusID:166221911.

[72] Klarmann N, Zoller B, Sattelmayer T. Numerical modeling of co-emissions for gas turbine combustors operating at part-load conditions. J Glob Power Propuls Soc 2018;2:C3N5OA. http://dx.doi.org/10.22261/JGPPS.C3N5OA.

[73] Klarmann N, Sattelmayer T, Geng W, Magni F. Flamelet generated manifolds for partially premixed, highly stretched and non-adiabatic combustion in gas turbines. In: 54th AIAA aerospace sciences meeting. 2016, p. 17592–605. http://dx.doi.org/10.2514/6.2016-2120.

[74] Goodwin D, Moffat H, Speth R. Cantera: An object-oriented software toolkit for chemical kinetics, thermodynamics, and transport processes. Version 2.2.0. 2015, http://dx.doi.org/10.5281/zenodo.48735.

[75] Poinsot T, Veynante D. Theoretical and numerical combustion. Prog Energy Combust Sci 2005;28.

[76] Tay-Wo-Chong L, Scarpato A, Polifke W. LES Combustion Model With Stretch and Heat Loss Effects for Prediction of Premix Flame Characteristics and Dynamics. In: Proceedings of the ASME turbo expo 2017: turbomachinery technical conference and exposition. Turbo expo: power for land, sea, and air, vol. 4A: Combustion, Fuels and Emissions, 2017, V04AT04A029. http://dx.doi.org/10.1115/GT2017-63357.

[77] Amerighi M, Nassini P, Andreini A, Orsino S, Verma I, Yadav R, Patil S. Assessment of flamelet generated manifold approach with inclusion of stretch effects of pure hydrogen flames. In: Proceedings of the ASME turbo expo 2023: turbomachinery technical conference and exposition. Turbo expo: power for land, sea, and air, vol. 3A: Combustion, Fuels, and Emissions, 2023, V03AT04A077. http://dx.doi.org/10.1115/GT2023-102651.

[78] Nassini PC, Pampaloni D, Meloni R, Andreini A. Lean blow-out prediction in an industrial gas turbine combustor through a LES-based CFD analysis. Combust Flame 2021;229:111391. http://dx.doi.org/10.1016/j.combustflame.2021.02.037.

[79] Celik IB, Cehreli ZN, Yavuz I. Index of Resolution Quality for Large Eddy Simulations. J Fluids Eng 2005;127(5):949–58. http://dx.doi.org/10.1115/1.1990201.

[80] Cavaliere DE, Kariuki J, Mastorakos E. A Comparison of the Blow-Off Behaviour of Swirl-Stabilized Premixed, Non-Premixed and Spray Flames. Flow, Turbul Combust 2013;91(2):347–72. http://dx.doi.org/10.1007/s10494-013-9470-z.

[81] Cerutti M, Giannini N, Ceccherini G, Meloni R, Matoni E, Romano C, Riccio G. Dry low NOx emissions operability enhancement of a heavy-duty gas turbine by means of fuel burner design development and testing. In: Proceedings of the ASME turbo expo 2018: turbomachinery technical conference and exposition. Turbo expo: power for land, sea, and air, vol. 4B: Combustion, Fuels, and Emissions, 2018, V04BT04A029. http://dx.doi.org/10.1115/GT2018-76587.

[82] Meloni R, Gori S, Andreini A, Nassini PC. CO Emission Modeling in a Heavy Duty Annular Combustor Operating With Natural Gas. J Eng Gas Turb Power 2021;144(1):011011. http://dx.doi.org/10.1115/1.4052028.